Apparatus for the lifetime measurement of Samarium excited states

by

Bahram Mojarrabi B.Sc.(Hons)

Thesis submitted for the degree of Master of Science

in the

Faculty of Science

University of Adelaide

March 1996

CONTENTS

Abstract

This thesis describes the construction of the apparatus for the measurement of the lifetime of the $^9F_1$ level of Samarium by the Hanle effect. The construction work involves the design and building of the vacuum system, the magnetic coils and the laser frequency stabiliser instruments. The project involved the assembly of the oven and the fluorescence signal detection system in addition to the direct calibration of the diode laser wavelength. A technique known as Optogalvanic spectroscopy was used to calibrate the laser wavelength. The basic properties of DC discharges and in particular the Samarium -Neon Hollow Cathode discharges are also reviewed.

The theory of Hanle effect in a three-level V-system is also presented.

A new method for the detection of the atomic beam of some materials is presented.

DECLARATION

I certify that this thesis does not contain without acknowledgement any material previously submitted for the award of a degree or diploma; and that to the best of my knowledge and belief it does not contain any material previously published or written by another person except where due reference is made in the text.

I give my consent to this copy of thesis being made available for photocopying and loan if accepted for the award of the degree.

.....

Bahram Mojarrabi

BSc (Hon)

Acknowledgements

I wish to thank my supervisor Dr M.W Hamilton for his help and support throughout the research of this thesis.

The guidance and advice of Dr D. McCoy at several stages throughout the course of this project has been greatly appreciated.

I'd sincerely like to thank Professor Jesper Munch for his help and the critical reading of the thesis. I extend my gratitude to Dr Peter Veitch for allowing me to use his personal computer.

Thanks also to Professor J.R Prescott and Mr Peter Berry-Smith for their contribution in the development of guidelines regarding the safe handling of the Samarium.

I would also especially like to thank Mr Laurentiu Stamatescu and Mr Peter Atanackovic, Dr Chaangjiang Weil and Ms Kerry Corbett for their effective suggestions and help.

I also express my gratitude to Dr Ursula McGowan of the ACUE and Ms Kerry Corbett for their help with the English grammar .

I also wish to express my humble gratitude to Mr Bob Hurn, Mr John Schache and Mr Blair Middlemiss and most importantly Mr Bob Nation and Mr Graham Eames for their enormous help in the construction of the Apparatus.

I also gratefully acknowledge the help from Mr John Smith and Mr Michael Shorthose with the construction of the electronic apparatus and invaluable technical assistance.

Many thanks also goes to the members of the optics group, especially Mr Vladimyros Devrelis, Robert Purviskis, Dr Yuri Matyagin, and Mr Armin Ardekani for their friendship and their helpful discussions.

I also wish to thanks Mrs Arlene Shaw, Ms Carmel Palumbo, Mrs Margaret Whiteford, Mrs Heather Duff and Mrs Mary Genovese for their beautiful smile s and kind heart s. Thanks also to Sharon Frecken and Tanya Weir for keeping us in touch with the letters.

I also extend my thanks to Ms Quyen Nguyen and Mrs Pamela Vogiatzis, my dear friends for their help in organising the manuscript.

I am deeply grateful to my perfect wife my dear Yae and my beautiful mother, brother and sisters. My pen is unable to fully describe their beauty.

Errata

abstract, line 2) '....the $^9F_1$ level....' should be changed to '....the $4f^6$ 6s 6p $^9F_1$ (14863.85 cm^{-1})....'

page 11, line 8) '*It is the time in which ....*' should be changed to '*It is the rate in which.....*'

page 21, line 20) '..... *on the absorption coefficient.*' should be changed to '*....on the laser intensity .*'

page 27, lines 14-15) '*....depends on Lande g factor as well as hyperfine g factor.*' should be changed to '*....depends on the hyperfine g factor as well as Lande g factor.*'

page 28, last line) '*....for the Earth's magnetic field.*' ~~should be changed to~~ '*....for the Earth's magnetic field as well as the stray magnetic field from the oven.*'

page 33, line 15) ' *....ionisation cross section....*' should be changed to ' *....ionisation probability....*'

page 87, line 6) ' *....steady state values of* $\sigma^{++},\sigma^{--},\sigma^{+-}$ *into....*' should be changed to ' *....steady state values of* σ^{++},σ^{--} *into....*'

page 87, line 8) '*.....algebraic manipulation, one can....*' should be changed to '*....algebraic manipulation involving equation (A 1.4), one can.....*'

h	Planck's constant
$\hbar$	$\frac{h}{2\pi}$
H	total Hamiltonian
I	laser intensity
I_s	saturating intensity
I_{nuc}	nuclear moment
i	current
J	total angular momentum
J_e	electron current density
J_{ion}	ion current density
L_c	cavity length
L	inductance
l	the length of the coil
λ	wavelength of the transition
$\|m\rangle$, m	Zeeman eigenstates
m	magnetic moment
m_e	electron mass
M	metastable level
M	magnetisation
μ_B	Bohr magneton
μ	magnetic permeability
μ_r	relative permeability

N	number of the turns of the coil
ω_l	Larmor frequency
ω	Laser frequency (angular)
P	pressure
P	power of the laser
R	mirror reflectivity
R	resistor
R_B	ballast resistor
R_g	generator resistor
r	coil radius
ρ	density matrix
ρ_r	reflection coefficient
S	cross section area of the coil
T_e	electron temperature
τ	lifetime
θ	angular divergence of the atomic beam
η	electron mean free path
υ	interaction Hamiltonian
V	Potential
υ_L	frequency of the laser
V_{sn}	shot noise amplitude
V_o	power supply voltage

Vref	reflected wave amplitude
ϑ	mean velocity of the atomic beam
w	Rabi frequency
χ_m	magnetic susceptibility
Z_l	load impedance

CHAPTER 1

Introduction

1.1) General introduction

The interaction of electromagnetic radiation with atoms is one of the most important aspects of modern physics. Apart from the absorption and emission of the light quanta, the interaction of electromagnetic radiation with matter may result in *interference of atomic states.*

Research on interference phenomena of the atomic states can be traced back to 1923 with the work of Hanle on the influence of a magnetic field on the polarisation of resonant emission [1]. The explanation of the interference phenomenon is based on the superposition principle. In accordance with the superposition principle, the wavefunction of the atom can be represented in the form of an expansion over eigenstates of a certain operator. The coefficients of this expansion are complex numbers. Their mean square moduli denote the probability of observing the system in certain eigenstates of the operator under consideration; i.e. they describe the population of states. The phases of these complex coefficients also have important physical meaning. They describe the

actual phase relation between the eigenstates of the operator. The density matrix ρ of the atom can be constructed from the products of these coefficients [2]. In chapter 2, we will discuss in detail how we can construct the density matrix from the principle of superposition. The time evolution of the density matrix can then be used to describe the interference phenomenon under consideration; i.e. the Hanle effect .

Interfering states in quantum systems of atoms or molecules can be observed by illumination with polarised light. Interaction of the exciting polarised light with the ensemble of atoms would establish a definite phase relationship or coherence between the interfering states (for all the atoms of the ensemble). The induced coherence between the atomic states can be mathematically interpreted as the density matrix having at least one non-vanishing off-diagonal element [3]. The coherence is a measure of the interference between the atomic states as it measures the degree of random noise which exists in the phase difference between the off-diagonal elements of the density matrix [4].

The techniques used to induce the coherence in atomic system are extremely diverse and a discussion of all of them is beyond the scope of this thesis. However one such technique is *optical pumping* [5]. By optical pumping we refer to a process in which atomic populations redistribute under the influence of incident radiation. Figure 1.1 shows how optical pumping can be used to create coherence in $|j=1\rangle$ level. Magnetic sublevels $|m=-1\rangle$ and $|m=+1\rangle$ are simultaneously excited by absorption of linearly polarised light (combination of σ^+ and σ^- polarised light). As a result a definite phase relation (coherence) is established between these sublevels and their fluorescence decay interfere·

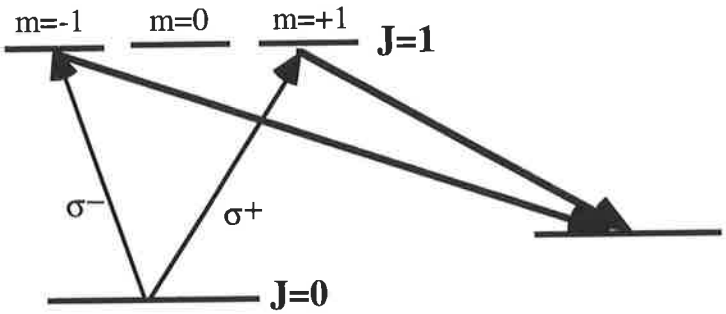

Fig 1.1: Level scheme for optical pumping of Zeeman sublevels by linearly polarised light.

The simplest systems where optical pumping can be applied are the V-shaped and Λ-shaped three level systems [6]. (see fig 1.2)

In the case of the V-configuration, optical pumping by linearly polarised light simply pumps a significant proportion of the ground state atoms into a coherent superposition of the excited sublevels. The decay fluorescence is polarised and its intensity varies with viewing direction. However when the degeneracy of the Zeeman sublevels is lifted by applying a controllable magnetic field, the coherence decreases and so the polarisation of the emitted radiation and its intensity in a given direction will change. The interference phenomena which appears is the *Hanle effect* (Zero field level crossing). (see fig 1.3a)

In practice, one scans the magnetic field around zero and observes the changes in polarisation or intensity of the emitted light to obtain the so called Hanle curve. Figure 1.3b shows a typical Hanle curve or Hanle signal. The full width at half maximum (FWHM) of the Hanle curve ΔB is related to the life time τ of the energy level [7].

$$\tau = \hbar/(g_J \mu_B \Delta B) \qquad \textbf{(1.1)}$$

where g_J is the Lande g factor of the excited level and μ_B is the Bohr magneton.

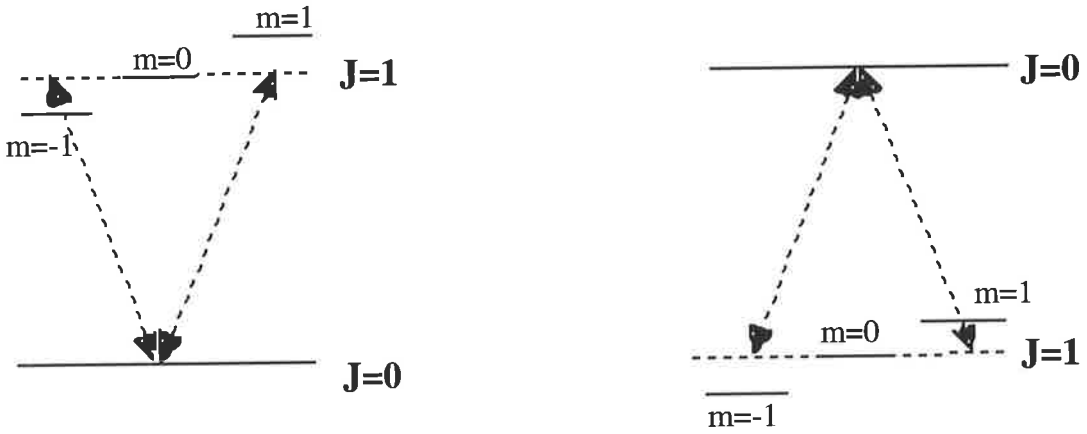

Fig 1.2: Three level systems V and Λ. A magnetic field is applied to lift the degeneracy of the Zeeman sublevels levels. In the V-configuration the m=0 state can not be populated by the linearly polarised light and so the V-system can be assumed to be an ideal three level system (ideal means only 3 levels are involved and all the losses occur within the 3-level system). However, one can not ignore the importance of m=0 of the lower level in the Λ-system. Although the m=0 state of the J=1 lower level is not driven by the linear polarised laser beam, it can be populated by spontaneous emission from the upper level. Therefore in the absence of collisions, the m=0 lower state traps some of the population of the Λ-system and thus for a realistic modelling of such systems the losses to the m=0 lower level should also be considered [8].

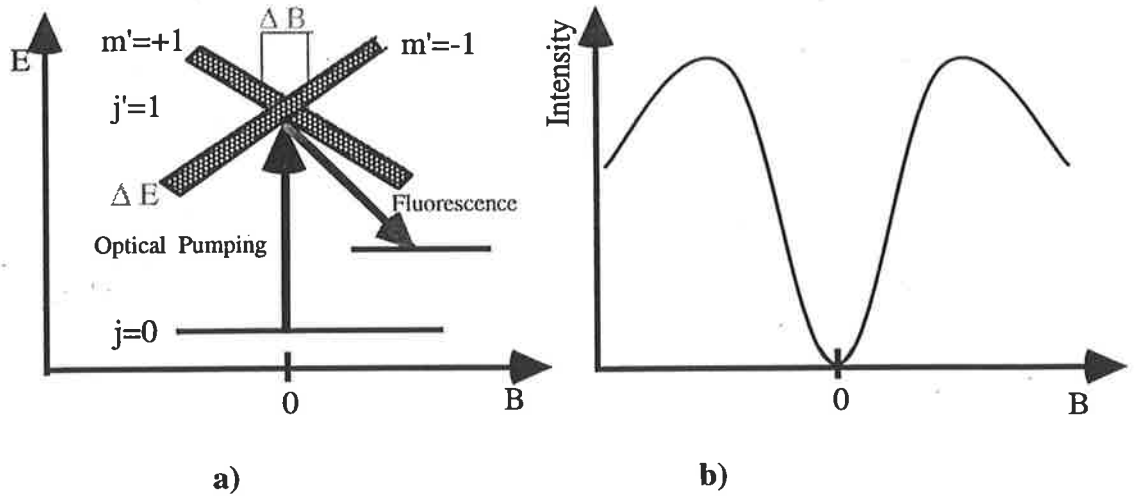

Fig 1.3: a) A typical Hanle effect in a V-system and b) its detected signal

The conditions required to obtain such a typical Hanle effect will be described in section 2.3.3.

In the Λ−system, when the frequency splitting of the Zeeman sublevels is equal to the frequency difference between two modes of the laser exciting beam then optical pumping by linearly polarised light causes the non absorbing coherent superposition of the Zeeman sublevels $|+1\rangle$ and $|-1\rangle$ (i.e. $\frac{1}{\sqrt{2}}(|-1\rangle - |+1\rangle)$)[9].

An atom left in such a superposition of states can no longer absorb or emit light, due to the destructive interference between the dipole matrix elements $\langle +1|P|0\rangle$ and $\langle -1|P|0\rangle$. As a result a narrow dip (a black line) in the Hanle curve appears whose width is extremely small. These black lines are very sensitive to the frequency detuning of the radiation fields and subsequently to the changes in the strength of the applied static magnetic field [10].

This interference phenomenon which was first observed in 1976 is called *Coherent Population Trapping* (CPT) or *dark line effect* and has

become the subject of very active research [29]. To a large extent the attraction stems from the very wide range of possible applications of this effect. They are namely: *ultra high- resolution spectroscopy, optical frequency standards, lasers without population inversion and the laser cooling of atoms* [11]. I will briefly discuss the cooling of the atoms by CPT in the next chapter.

Studies of the effects of the laser noise on coherent population trapping systems are essential in the development of these applications. Such studies have become feasible by the development of techniques that enable the investigators to impose on the laser a statistically well characterised noise such as Gaussian and/or Dichotomous noise. Gaussian noise, whose random variable has a normal distribution, has been added to the laser phase and amplitude [12]. Dichotomous or random telegraph noise have been imposed on the laser phase and frequency. This noise consists of random jumps between two allowed levels of the noise parameter (phase or frequency) and can be described in terms of its auto correlation function [13].

The experimental research on the effect of the noise on the coherence induced in CPT, requires the selection of an appropriate ensemble of atoms. Samarium (Sm) was selected in the project as an ideal element on which to carry out future CPT studies. Their first three ground state fine-structure multiplet (in which we are interested) are well- populated thermally in the atomic beam. It is an atom in which L-S coupling holds and also has suitable levels in which Λ-systems can be formed. For example $4f^6\,6s\,6p\ ^9F_1$(14863.85 cm^{-1})and $4f^6\,6s^2\ ^7F_1$ (293.58 cm^{-1}) levels show the essential features of a Λ-system. The $^9F_1$ and $^7F_1$ levels each have 3 magnetic sublevels. The Λ-system of interest is comprised of lower $m = \pm 1$ and upper $m = 0$ states as shown in figure 1.4a.

The lifetime of the upper level $^9F_1$ can be measured with the aid of the Hanle effect. The 672.58 nm transition forms the V-system which we can use to observe the Hanle effect on the $^9F_1$ level. (see figure 1.4b)

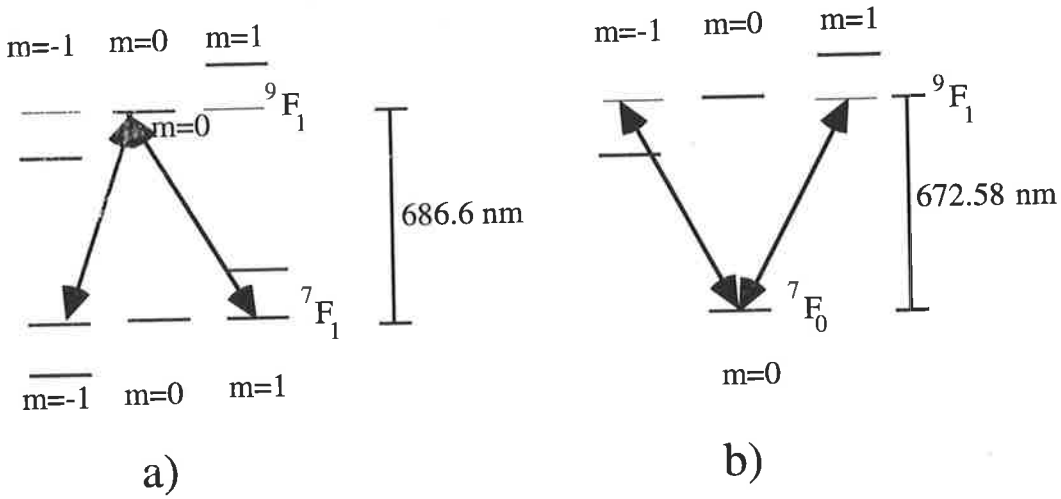

Fig 1.4: (a) The Λ-system with $^9F_1$ level as its upper level (b) The V-system which allow us to measure the lifetime of $^9F_1$.

The specific aims of my project were, firstly, to construct the apparatus for the life-time measurement of the $^9F_1$ of Sm based on the Hanle effect and, secondly to calibrate the diode laser wavelength. The method of calibration was based on optogalvanic spectroscopy. It involves monitoring the change in impedance of a gas discharge caused by irradiation of the discharge plasma by light whose frequency matches a transition frequency in the atoms or ions which constitute the plasma [14].

1.2) Scope of the thesis

In chapter 2, I will present the phenomena of level crossing as an interference of the atomic states. I will describe the emission from a classical dipole oscillator in a magnetic field and examine the characteristics of such an emission. I will also use the density matrix concept in quantum mechanics to explore the phenomena of zero field level crossing with laser light as an excitation source. The derivation is based on the V-configuration and enables us to derive the equation necessary for measuring the Hanle effect. The extension to the Λ-system will be discussed. In the end of chapter, I will suggest the steps necessary for the measurement of the lifetime of the $^9F_1$ level by Hanle effect.

In chapter 3, I will discuss the basic properties of a DC discharge and describe the conditions in which optogalvanic spectroscopy can be used to measure the laser bandwidth. I will also discuss a model which predicts the polarity of the signals in a Sm-Ne discharge.

In chapter 4, I will discuss the design and construction of the apparatus and present the experimental procedure for the detection of the signal. As part of the design, I will critically consider the influence of factors such as laser power, its frequency stability and bandwidth , the atomic beam density and its collimation in the construction geometry. This ensures that experimental results will be taken under optimum conditions. At the end of the chapter, I will present the analysis of the data obtained by OPG spectroscopy.

CHAPTER 2

Mathematical description of the Hanle effect

2.1) Introduction

The object of this chapter is to develop the theoretical work necessary to explain the Hanle signal .

Section 2.2 is devoted to a qualitative discussion about the classical treatment of the Hanle effect.

In section 2.3, we discuss the semi-classical formalism of the Hanle effect. In the derivation the excitation light will be treated as a classical field while the atom will be treated as quantum mechanical entity with discrete energies. We start our discussion by introducing the density matrix and proceed with a brief discussion on the applicability of the rate equation. I conclude that for a monochromatic laser it is necessary to use the Liouville equation which includes the optical coherence elements of the density matrix between ground and excited state.

In section 2.3.2 I will use the Liouville equation to describe the Hanle signal with monochromatic excitation . In section 2.3.4 I discuss the extension of the formalism to the Λ – system.

In section 2.4, I will review the experimental factors which may influence the shape of the Hanle signals.

In section 2.5, I suggest the experimental steps for obtaining the Hanle curve.

In the last section, I will briefly look at some of the most important applications of zero field level crossing.

2.2) Classical treatment

The classical treatment of the Hanle effect has appeared in many publications [1,5,15,16]. Hanle used this approach to describe his first experiment on the polarisation of resonance fluorescence in the presence of a magnetic field [7].

I will show that the phenomena of zero field level crossing is the result of the interference between different components of the classical dipole radiation.

To do so, it is appropriate to start our discussion with a consideration of the electron oscillator in the Lorentz model (see fig 2.1a) [17]. In such an approach, we must consider the coupling between an electron and the residual ion core by a quasi elastic force which acts to restrain the system in an equilibrium position. In the Lorentz model, there is no quantitative explanation for the elastic forces that restrain the electron to the equilibrium position. In this sense, it is an incomplete model [18]. At equilibrium, the centres of the positive and negative charges coincide, and consequently, the system will have a zero dipole moment. Under the influence of an electromagnetic field, the electron experiences the Lorentz force and is displaced from its equilibrium position. However, by the action of the quasi-elastic force, the electron will be pulled back to the equilibrium position and thus will undergo an oscillation about the

equilibrium position. From such oscillation, one can easily deduce a dipole moment oscillation at the optical frequency ω_o.

The polarisation of the dipole radiation depends on the direction of observation and the direction of the polarisation of the exciting radiation [5]. Figure 2.1b shows the radiation pattern of a dipole.

However, a real emitting dipole radiates energy and so its oscillation is damped. The solution for such an oscillation will involve a damping constant Γ. It is the time in which the radiation from the dipole decreases by a factor 1/e. In quantum mechanical language it is the reciprocal lifetime of the energy level and is called the natural width of the energy level. [15]

When such a dipole is placed in a magnetic field which is applied along the z axis, the motion of the dipole is subject to an external Lorentz force. The equation of motion is similar to the equation of forced oscillator motion and can be decomposed in 3-dimensional Cartesian co-ordinates. Its solution consists of 3 projection components of oscillation of the dipole on the 3-d Cartesian axes. The **z** component of the oscillation will not be effected by the magnetic field and so will have the same angular momentum as the free dipole oscillator ω_o. The **x** and **y** components will, however, be influenced by the magnetic field. The Larmor frequency ω_l will add or subtract from their optical frequency ω_o according to the direction of their rotation about the field axis [5]. The net result is the precession of the dipole (or more accurately, the precession of the projection of the dipole in the **xy**-plane) about the magnetic field. (see fig 2.1 c)

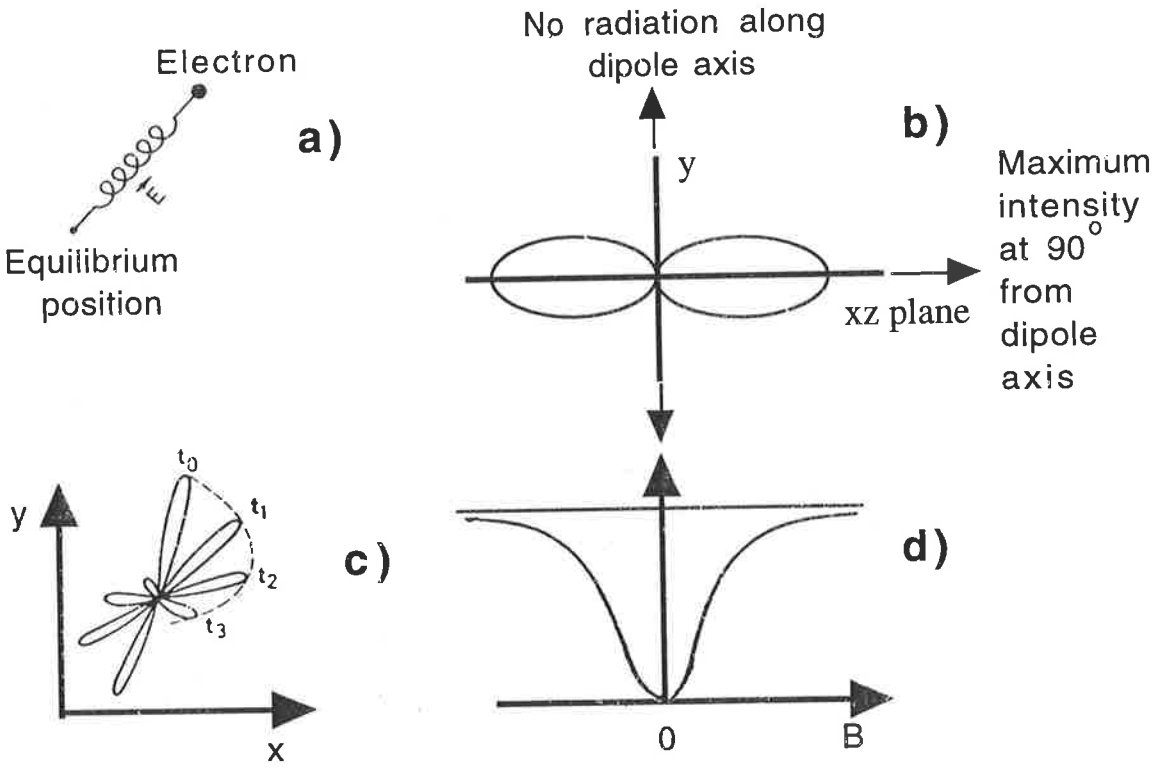

Fig 2.1: a) The electron oscillator [18] (b) Dipole radiation pattern (c) the intensity distribution of the dipole at different times t, due to precession of the dipole in an external magnetic field parallel to **Z** direction. (d) A typical Hanle effect by broadband excitation (with polarisation of the excitation light along **y** axis). The detector is along **y** axis with polarisation along **x** axis.

As the magnetic field changes, the rate of the precession of the dipole about the magnetic field axis will be changed. Consequently the intensity reaching an observer will vary in time. The intensity variation can be described as the result of the interference of the radiation between different components of the dipole; i.e. the radiation from the component along the magnetic field with the emission from a rotator in the x-y plane. The intensity variation consists of two frequencies: the Larmor frequency ω_l and twice the Larmor frequency $2\omega_l$ [5].

Experimentally, the time variation of the intensity at twice the Larmor frequency can be observed in time resolved experiments in which the dipoles are subject to pulse excitation. However, in the Hanle effect experiments one is concerned with steady-state experiments in which there is no time variation of intensity. In such experiments, the dipoles are excited at random times or at a constant rate of excitation and we observe their radiation continuously from $-\infty$ to the time of observation t [15]. At low values of the field, the Larmor precession is small and the dipole radiation lobe decay before a full revolution and the observer will record little light. As the magnetic field increases, the number of times that the dipole lobe passes in and out of the detector (during its decay time) increases and so the observer registers more light. For still higher fields, the lobe illuminates the detector many times before it decays. As a result the signal levels off at a limiting value. The situation is shown in figure 2.1d [19].

2.3) Semi-classical formalism

The density matrix is the most appropriate tool for a semiclassical treatment of interference phenomena. The reason is that its formalism reflects not only the experimental situation of a collection of atoms with same pure state but also in a mixed quantum state [20].

2.3.1) Density matrix

The state of an atom at a particular time t can be described by state vector (wave function) $|\Psi(t)\rangle$. The state vector can be represented as a superposition of eigenstates $|\phi_n\rangle$ of a certain operator:

$$|\Psi(t)\rangle = \sum_n a_n |\Phi_n\rangle \qquad (2.1)$$

Here n refers to a given set of quantum numbers which distinguishes between different eigenstates. The probability amplitudes a_n are, in general, complex.

Since the form of $|\phi_n\rangle$ is known, then all information about the state of the atom before and after an interaction can be found by *measuring* the amplitudes a_n. When all the relevant coefficients a_n are found experimentally, then we refer to the experiment as being complete. A complete experiment can be designed to act as a filter which leaves the system undisturbed. The state of such a system is called a pure state [22].

Suppose that we have collected a large number of atoms, all of which are in the same pure state. All observable quantities of this system correspond to the expectation values of its operators. The expectation value of an operator Q corresponding to the observable quantity in the experiment is given by :

$$\langle\Psi|Q|\Psi\rangle = \sum_{n,k} a_n a_k^* \langle\Phi_k|Q|\Phi_n\rangle \qquad (2.2)$$

The table of the coefficients $a_n a_k^*$ in equation 2.2 is defined as density matrix ρ_{nk} or simply ρ.

The diagonal elements $\rho_{nn} = a_n a_n^*$ describe the population of states;

they determine the probability of observing the system in the state Φ_n. The off-diagonal elements describe the phase relationship between different eigenstates and are called interference or coherence terms [5].

Now suppose that the atoms in the sample have a mixture of states $|\Psi_1\rangle,|\Psi_2\rangle,...|\Psi_\alpha\rangle,...|\Psi_n\rangle$. For example, the atoms in the atomic beam have different velocities. The density matrix of such a system is given as a sum: $$\rho = \sum_{\alpha} P\alpha\rho^{\alpha}.$$

Where P_α is the probability that an atom belongs to a certain sub ensemble α; i.e. the relative number of atoms in each state.

Since the density matrix contains all the physically observable information inherent in a quantum system, one can say that the density matrix determines the state of a system (in both pure and mixed ensembles) [5].

2.3.2) Application of the density matrix to the theory of the Hanle effect

The time evolution of the density matrix for an ensemble of atoms can be determined from the Liouville equation: [16]

$$\frac{d\rho}{dt} = \frac{1}{i\hbar}[\rho, H] + \hat{\Gamma}_\rho \qquad (2.4)$$

Where H is the total atomic Hamiltonian and includes the unperturbed Hamiltonian H_0 and the interaction Hamiltonian υ; i.e.

$$H = H_O + \upsilon$$

$\hat{\Gamma}_\rho$ is added to the equation to describe the effect of spontaneous emission. In an atomic beam environment, we can ignore the collision relaxation.

Experiments on lifetime measurements by the Hanle effect are usually performed using broadband excitation in which the spectral width of the incident beam is much larger than natural width of the atomic transition [5]. The wide spectral bandwidth of the excitation source means one can ignore the coherence between ground and excited state as the spatial and temporal coherence of the exciting light is small. In this case the density matrix does not contain any off-diagonal elements and so the density matrix ρ of the atom reduces to the sum of ground state and excited state density matrixes. The Liouville equation then reduces to a set of differential equations known as the rate equations. These rate equations depend on the level population, the magnitude of the dipole moment and the magnetic field strength. From the steady state solutions of these rate equations, one can derive the Berit-Franklin formula which can be used to describe the Hanle effect [16].

In the experiment, I used a free running diode laser with minimum bandwidth of about 9 MHz which is much greater than the natural width of the transition of interest (about 0.38 MHz). However, it is intended that the diode laser will be used in a grating external cavity arrangement. By using an external cavity M.G Bashier et al have shown that it is possible to reduce the linewidth of the laser to a few hundred kHz over a considerable length of time [22]. In this circumstance, the diode laser can be used as a monochromatic excitation source. For monochromatic excitation, the approach requires Liouville or Bloch equations which include extra terms such as dipole phase and laser electric field strength [23].

In this thesis, I will write the equation of motion of the density matrix for arbitrary values of the laser intensity in the dipole and rotating wave approximations for monochromatic excitation [16,24,25,26]. However, the steady state solution will only be found for the case of zero detuning

and also for the low intensity limit of the laser. We assume that all the atoms in the atomic beam which interact with the laser have the same velocity; i.e. all the atoms in the ensemble are in the same pure state.

2.3.2) The equation of motion of the density matrix

The equations of motion of the components of the density matrix presented in this section have been derived and comprehensively discussed by Avan and Cohen-Tannoudji [25].

Consider the geometry in fig 2.2. The magnetic field is along the **z** axis. The atoms are irradiated by a single mode laser beam with frequency ω. I have supposed that the laser frequency is in resonance with the atomic frequency ω_o; i.e. $\omega = \omega_o$. The laser beam has a linear polarisation (combination of two σ components of circularly polarised light) $\mathbf{e_y}$ parallel to the **y** axis and travels along the **z** axis. The atomic beam is propagating along the **x** axis. The symmetrical Hanle effect signals can be observed in two detection channels. The observer can detect fluorescence light along the **y** axis with a linear polarisation $\mathbf{e_x}$ or along the **x** axis with the linear polarisation $\mathbf{e_y}$.

Consider the case in which the atom is characterised by two energy levels(the lower and the upper). The simplest system, in which one can observe the Hanle effect, is the V-system involving a J=o→ J=1 transition.

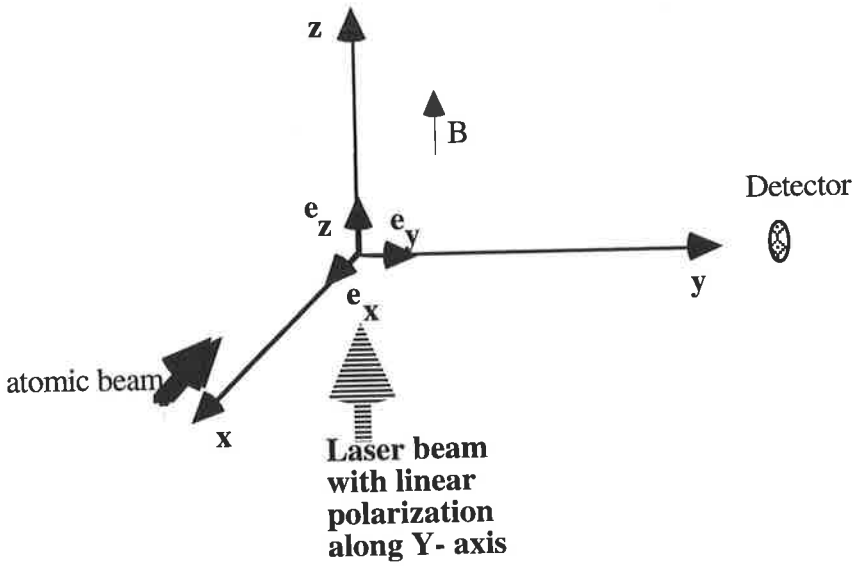

Fig 2.2: Schematic diagram of the geometry of the system.

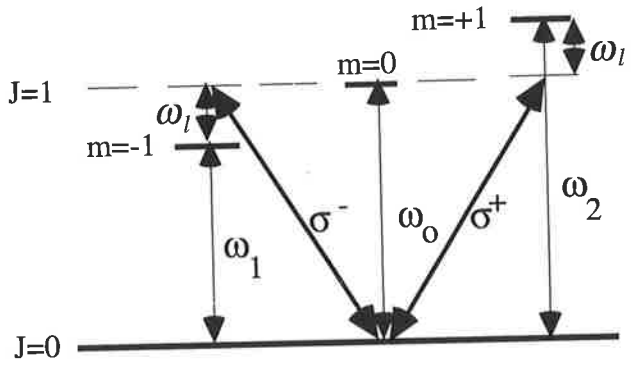

Fig 2.3 : Monochromatic excitation of the Hanle effect. The excitation laser beam is linearly polarised. $\omega_o = \frac{\omega_1 + \omega_2}{2}$ and $\omega_l = \frac{\omega_2 - \omega_1}{2}$.

As the polarisation of the laser light $\mathbf{e_y}$ is perpendicular to the magnetic field direction, then σ^+ and σ^- can stimulate $|+1\rangle$ and $|-1\rangle$ states. We consider <u>only</u> $|0\rangle \leftrightarrow |+1\rangle$ and $|0\rangle \leftrightarrow |-1\rangle$ transitions which correspond to frequencies $\omega_o+\omega_l$ and $\omega_o-\omega_l$ respectively. Here $\omega_l = \frac{\omega_2 - \omega_1}{2}$ is the Larmor frequency of the excited state and

$\omega_o = \frac{\omega_1 + \omega_2}{2}$ is the frequency of the optical transition in zero magnetic field. (see fig 2.3)

In equation 2.4, the diagonal elements of $\hat{\Gamma}\rho$ denote the population decay of the upper state at a rate Γ equivalent to the natural width of excited state level. The off-diagonal elements ρ_{+-} , ρ_{-+} of the density matrix ρ will decay also at the rate Γ. However the off-diagonal elements ρ_{+0} , ρ_{-0}, ρ_{0+} and ρ_{0-} will decay at half the rate of the upper state as the ground state damping constant is assumed to be very small (i.e. ≅ zero). We have ignored collision relaxation.

The unperturbed operator H_o will not induce any coupling between the density matrix elements and so exists only for terms with the same index and is therefore diagonal.

The interaction Hamiltonian υ describes the interaction of the atom with the laser beam. We can apply the dipole approximation as the wavelength of the laser exciting light is much larger than the size of the atom. In the dipole approximation the interaction Hamiltonian υ has the form:

$$\upsilon(r,t) = -P_y \cdot E(r,t) \qquad (2.5)$$

where $P_y = e_y . P$ is the component of the electric dipole moment of the atom along the polarisation vector $\mathbf{e_y}$ and E(r,t) is the electric field of the linear polarised light which has the form:

$$E(r,t) = \frac{1}{2} E_o e^{-i\omega t} + c.c$$

here E_o denotes the mean amplitude of the electric field and is chosen to be real. The c.c is the complex conjugate term of the electric field. The intensity of the laser beam I is related to E_o via:

$$I = \frac{c\varepsilon_o}{2} E_o^2 \qquad (2.6)$$

where c is the speed of the light and ε_o is the vacuum permitivity . We substitute the eqn (2.6) into the equation for the E(r,t) to obtain:

$$E(r,t)=\sqrt{\frac{I}{2c\varepsilon_o}}(e_y e^{-i\omega t}+e_y^* e^{i\omega t}). \qquad (2.7)$$

Then the interaction Hamiltonian υ can be written in explicit form:

$$\upsilon=-\frac{\sqrt{I}}{\sqrt{2c\varepsilon_o}}\langle+|(e_y e^{-i\omega t}+e_y^* e^{i\omega t}).P|0\rangle-\frac{\sqrt{I}}{\sqrt{2c\varepsilon_o}}\langle-|(e_y^* e^{-i\omega t}+e_y e^{i\omega t}).P|0\rangle.$$

We choose the relative phases of the two excited sub levels $|+1\rangle$, $|-1\rangle$ with respect to the ground state $|0\rangle$ such that the two matrix elements $\langle+|P_y|0\rangle=\langle-|P_y|0\rangle$ are real and positive to get:

$$\upsilon=-\frac{\sqrt{I}}{\sqrt{2c\varepsilon_o}}(e^{-i\omega t}+e^{i\omega t})(\langle+|e_y.p|0\rangle+\langle-|e_y.p|0\rangle). \qquad (2.8)$$

We define the *Rabi frequency* w as:

$$w=-\frac{1}{\hbar}\sqrt{\frac{I}{2c\varepsilon_o}}\langle+|e_y.p|0\rangle=-\frac{1}{\hbar}\sqrt{\frac{I}{2c\varepsilon_o}}\langle-|e_y.p|0\rangle. \qquad (2.9)$$

In matrix notation, ρ, H_o , υ and $\hat{\Gamma}\rho$ have the following forms:

$$\rho=\begin{bmatrix}\rho_{++} & \rho_{+0} & \rho_{+-}\\ \rho_{0+} & \rho_{00} & \rho_{0-}\\ \rho_{-+} & \rho_{-0} & \rho_{--}\end{bmatrix},$$

$$\upsilon=\hbar\begin{bmatrix}0 & w(e^{-i\omega t}+e^{i\omega t}) & 0\\ w(e^{i\omega t}+e^{-i\omega t}) & 0 & w(e^{i\omega t}+e^{-i\omega t})\\ 0 & w(e^{-i\omega t}+e^{i\omega t}) & 0\end{bmatrix},$$

$$H_o=\hbar\begin{bmatrix}\omega_o+\omega_l & 0 & 0\\ 0 & 0 & 0\\ 0 & 0 & \omega_o-\omega_l\end{bmatrix},$$

$$\hat{\Gamma}\rho=\hbar\begin{bmatrix}-\Gamma\rho_{++} & -\frac{1}{2}\Gamma\rho_{+0} & -\Gamma\rho_{+-}\\ -\frac{1}{2}\Gamma\rho_{0+} & \Gamma(\rho_{++}+\rho_{--}) & -\frac{1}{2}\Gamma\rho_{0-}\\ -\Gamma\rho_{-+} & -\frac{1}{2}\Gamma\rho_{-+} & -\Gamma\rho_{--}\end{bmatrix}$$

As we show in appendix 1, the steady state solution for the fluorescence $L_f(e_y)$ emitted along y-direction with zero detuning is:

$L_f(e_y)=$

$$\frac{4\alpha\omega_l^2 w^2 F^2}{4w^2\omega_l^2(\alpha F + w^2 + 3\alpha^2) + \Gamma^2 F(Fw^2 + \alpha(4F + \alpha\omega_l^2 + w^2 + 4\alpha) + 4\alpha^3\omega_l^2}$$

(2.10)

where $\alpha = (\frac{\Gamma}{2})^2 + \omega_l^2$ and $F = \alpha + w^2$

It can be seen from eqn 2.10 that the Hanle signal $L_f(e_y)$ depends on the static magnetic field (via ω_l) and the laser intensity (via Rabi frequency w^2).

An increase in the intensity of the laser increases the total decay rate of population of the upper and lower levels due to the enhancement of the stimulated emission and absorption. Therefore the linewidths of the upper and lower levels are broadened. The effect which is called power broadening would result in the widening of the width of the Hanle curves [27]. Figure 2.5 shows the increase of FWHM of the signals due to power broadening effect. The different curves correspond to the different values of the laser intensity.

At very high laser intensity, in which the intensity of the laser is equal or higher than the saturation intensity I_s (see appendix 2), the Hanle signal is strongly power broadened and its profile also shows a nonlinear dependency on the absorption coefficient. This phenomenon, which is called the nonlinear or saturation Hanle effect (NLHE), would prevent us from measuring the lifetime of the excited level from the HWFM of the Hanle curve. A detailed discussion about the NLHE can be found in the references [16,7]. Therefore, for the measurement of the lifetime by the laser excitation, we should look in the region of low laser intensities.

At vanishing laser intensity, we keep only the lowest order of Rabi frequency w, in eqn 2.10. In this case the signal would have the following form:

$$L_f(e_{y)} = w^2(1 - \frac{(\frac{\Gamma^2}{4})^2}{(\frac{\Gamma^2}{4})^2 + (\omega_l^2)^2}) \qquad (2.11)$$

The above equation for the fluorescent intensity has an inverted Lorentzian shape for which its FWHM is equal to half the width of the excitation light in the broadband case (see figure 2.5). Rasmussen et al were the first to measure the lifetime of the excited state by using a monochromatic laser with vanishing light intensity [28].

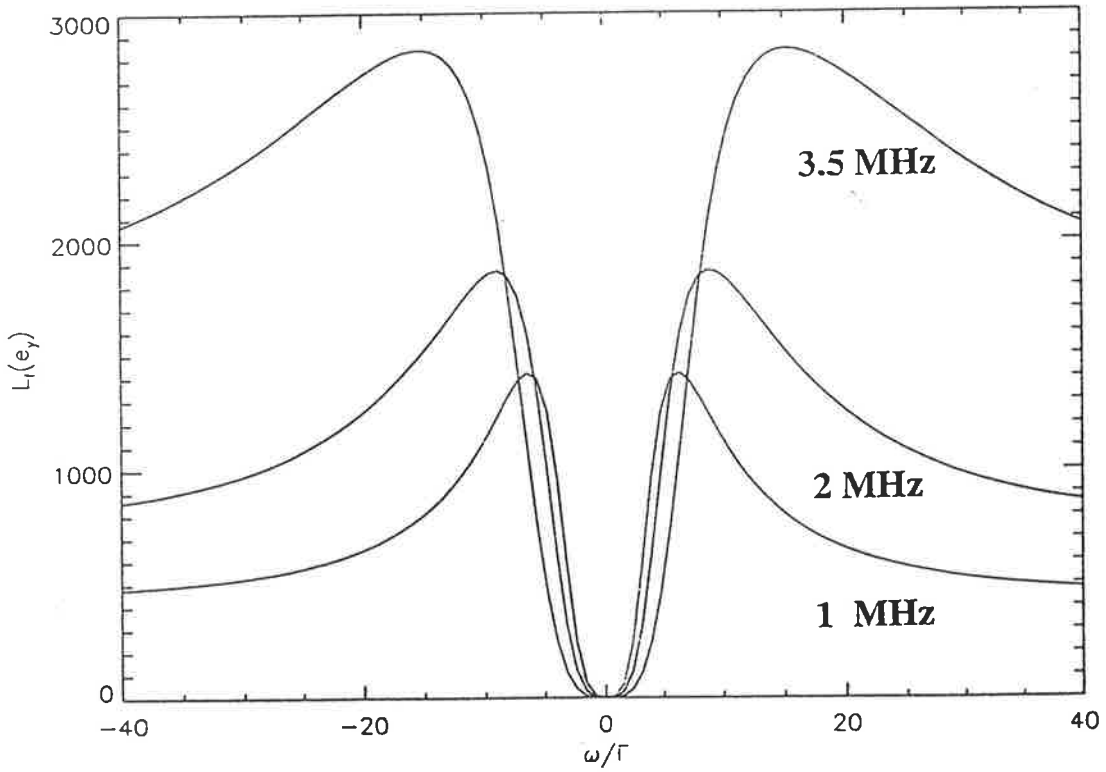

Fig 2.4: Set of zero field level crossing resonances detected on L_f(ey) for a zero detuning in a three level system. One clearly sees a power broadening of the resonances. Each curve corresponds to a different value of the Rabi frequency.

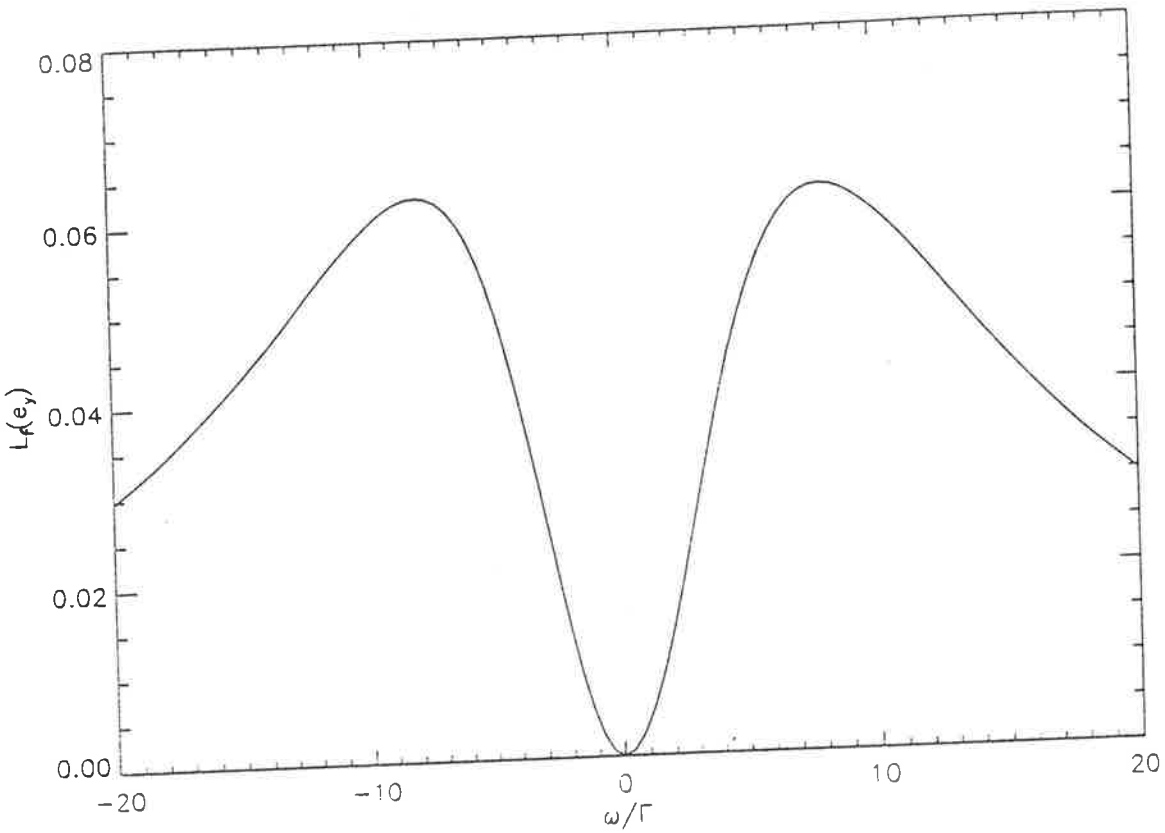

Figure 2.5: A typical Monochromatic excited Hanle signal in the low intensity limit . The FWHM of the signal is approximately narrower by a factor of 2 relative to broad band excitation. At higher magnetic field the tails tend to zero. This is due to fact that the frequencies $\omega_o \pm \omega_l$ of the transition lines $|0\rangle \leftrightarrow |+1\rangle$ and $|0\rangle \leftrightarrow |-1\rangle$ are out of resonance with the laser frequency ω. For broadband excitation the tails would level off at a constant value (see figure 2.1.d) [25].

2.3.4) Extension to Lambda system

The discussion so far was centred on the Zeeman coherence effect in the V-system. However, the effect is similar in the Λ-system if one modifies the equations of motion [29].

The relaxation terms must be changed in accordance with the relaxation process of the Λ-system. In this case the matrix $\hat{\Gamma}_\rho$ will have the following form:

$$\hat{\Gamma}_\rho = \begin{bmatrix} \Gamma\rho_{00} & \frac{1}{2}\Gamma\rho_{+0} & \gamma\ \rho_{+-} \\ \frac{1}{2}\Gamma\rho_{0+} & 2\Gamma\rho_{00} & \frac{1}{2}\Gamma\rho_{0-} \\ \gamma\ \rho_{-+} & \frac{1}{2}\Gamma\rho_{-0} & \Gamma\rho_{00} \end{bmatrix} \tag{2.11}$$

where Γ is the decay rate of the upper level and γ is the rate of relaxation of coherence of Zeeman sublevels .

The fluorescent decay depends on the population of the upper level ρ_{00} while for the V-system, the fluorescent decay depends on the population of Zeeman sublevels and to the coherence between them.

It is also important to note that, while the J=0 to J=1 transition can be treated as a ideal V-type three level system, the J=1 to J=0 transition can not be treated as a ideal Λ-type three level system due to the role the state m=0 of the lower level plays. As I mentioned in the introduction (see figure 1.2) for a realistic modelling of such systems, the spontaneous decay into the lower m=0 level should be also considered . However the effect of optical pumping into the m=0 lower level can be distinguished from the optical pumping into the lower level superposition state [30].

2.4) Conditions for observation of the zero field level crossing

The first condition for the observation of the zero field level crossing signal is the proper geometrical lay out. In fact level crossing experiments can be performed in a variety of geometrical arrangements. The geometry of the constructed apparatus is shown in figure 2.2.

An important experimental factor for the optimum observation of the Hanle signal is the minimisation of line-broadening sources such as the stray magnetic field, Holtzmark effect and line narrowing source such as coherence diffusion [27,3].

Holtzmark effect occurs as aresult of collisions between similar atoms in the ensemble and in general is not a problem in the atomic beam. Coherence diffusion or radiation trapping occurs when the emitted light from the excited state atoms is re-absorbed by the ground state atoms of the ensemble. Since the fluorescence emitted light carries information about the coherent state of the atom, the re-absorption of the light by other atoms in the ensemble increases the decay time. This would lead to the narrowing of the Hanle curve. Radiation trapping may cause problems in the atomic beam of some elements. In Sm the radiation trapping does not seem to cause any significant narrowing of the Hanle curve in the vapour density range of interest as reported by L. Marek et al [31]. However, since the effect of radiation trapping is different with different transitions, an experimental check is recommended [31a].

The collimation of the atomic beam is also an important experimental factor which affects the number of the atoms in the excited states [32,33]. To maximise the fraction of atoms in a given excited state within the absorption profile, the laser must intersect the atomic beam at right angles to eliminate longitudinal Doppler effect. However, a residual transverse velocity component will still remain due to the divergence of the Sm atomic beam and the finite line width of the laser beam. This velocity component will induce a shift of about

$$\Delta\nu_D = \frac{\vartheta}{\lambda}\sin\theta \qquad (2.12)$$

where ϑ is the mean velocity of the Sm atomic beam, λ is the resonance wavelength (672.58 nm) and θ is the angle of divergence of the Sm beam. In order to include the largest fraction of the atoms in the

absorption profile, this transverse Doppler spread should be smaller than the natural line width $\Delta\nu_{nat}$ i.e.

$$\Delta\nu_D \leq \Delta\nu_{nat} = 1/2\pi\tau \tag{2.13}$$

So in practice, in the design of the vacuum chamber, one should place the collimator aperture in a position which introduces the smallest possible divergence angle of the atomic beam. In our constructed chamber, for example , the divergence angle of the beam should be about 0.002 rad. In this ideal case, one expects to obtain $\approx 10^5$ scattered fluorescence photons per second at 3.8 mW laser power for 672.5 nm transition.

Stray magnetic field is another important factor that distorts the shape of the Hanle signals. The laboratory stray magnetic field affects the system in a complicated way depending on the geometry of the detection signal with respect to its direction. The major contribution to the stray laboratory magnetic field is the earth's magnetic field and the field produced by the oven current. In the constructed geometry the uncompensated component of the earth's magnetic field is along the direction of the applied magnetic field and so the position of the zero level crossing will be shifted by a certain amount equal to the earth's component field. However, the oven magnetic field is perpendicular to the direction of the applied magnetic field and parallel to the polarisation of the excitation light. The signal amplitude will be decreased and the shape of the Hanle curve will be distorted by this field. By constructing three Helmholtz coils perpendicular to each other one can produce a net magnetic field which completely nulls the effects of the stray magnetic field [34].

It is important to point out that the local field inhomogeneities over the interaction volume will produce significant shift and broadening of the Hanle resonances. A proper design of the main coil, which produces the applied external magnetic field, will minimise the effect of these

inhomogeneities on the measured lifetimes. In our work, we designed the main coil based on 3 factors discussed in A. E. Ruak and M. F. Peters 1926 paper [35]. They are summarised as: i) The minimum degree of field uniformity required over the interaction region; ii) The dimensions of the interaction region and iii) the field strength required. The field uniformity is a measure of the local inhomogeneities in the interaction region. It can be defined as the maximum amount the field at any point of the interaction volume is allowed to deviate from the value of the field at the centre [36].

The hyperfine structure will also affect the Hanle signals. The hyperfine structure causes depolarisation of the emitted radiation [5,15]. The hyperfine structure also causes a nonlinear dependency of the distance between the Zeeman sublevels to the applied magnetic field. In this case the signal width depends on the Lande g factor as well as hyperfine g factor. Two odd isotopes of Samarium m=147 and M=149 possess nuclear moment of $I_{nuc} = \frac{7}{2}$ which determines the hyperfine structure. For this project, we will work with ^{154}Sm which has zero nuclear spin.

The power density of the laser is another factor which affects the shape of the Hanle signals. In measurement of the lifetime of the excited state by monochromatic light, the laser intensity should be very small for equation 2.10 to be valid. In practice, it might not be desirable or even possible to lower the power of the laser to the required amount because of the difficulties in obtaining a proper signal at such a vanishing intensity. However, any increase in the power of the laser may result in the power broadening of the signal. The FWHM of the power broadened line profile is then: [33]

$$\Delta\upsilon_{broad} = \Delta\upsilon_{nat}\sqrt{1+\frac{I}{I_s}} \qquad (2.14)$$

where $$I_s = \frac{\pi hc}{3\lambda^3 \tau}.$$

and λ is the wavelength of the transition.

It is important to note that at significantly high laser intensity the measured HWFM can not be used to calculate the lifetime of the excited level. The reason is that the absorption coefficient of the atom will also change with magnetic field strength at such high intensities.

2.5) Suggested steps for determination of lifetime of excited state

1) Determine the bandwidth of the laser to see whether it is monochromatic.

2) Determine the intensity of the laser.

3) Turn on the vacuum system and when the pressure is less than 10^{-7} Torr, slowly turn on the oven.

4) Use the reflection pulse technique to detect Sm beam (see appendix 3).

5) Tune the laser in resonance with the transition. Note the wavelength of the line will be different in the vacuum compared with the data recorded in air.

6) Turn on the photomultiplier.

7) Maximise the intensity of the detected signal by fine tuning the laser wavelength, changing the degree of focusing of the laser , adjusting the laser beam direction and increasing the Sm atomic beam density.

8) Measure the frequency stability of the laser by recording the signal over time. When the intensity of the signal has considerably dropped, record the time taken. Make sure the oven has enough Sm.

9) Turn on the Helmholtz coils to compensate for the earth magnetic field.

10) Check the degree of polarisation of the excitation source.

11) Turn on the main coil.

12) Reduce the power of the laser and slowly change the value of the magnetic field by changing the current through the main coil. The time taken by the experiment should not exceed the time recorded in step 8).

13) Plot the resulting measured intensity versus magnetic field .

14) Deduce the amount of power broadening of the signal.

15) Compare the experimentally fitted curve (at zero detuning) with the theoretical curve obtained from eqn 2.10.

16) Obtain the Hanle curve for different values of detuning $\Delta\omega = \omega - \omega_o$ and compare it with the theoretical curve obtained from equation 2.11 which include the detuning [25].

$$L_f(e_{yy}) = \frac{w^2\omega_l^2}{[(\frac{\Gamma^2}{4} + (\Delta\omega - \omega_l)^2][(\frac{\Gamma^2}{4} + (\Delta\omega + \omega_l)^2]} \qquad (2.15)$$

17) Add all the signals obtained from steps 15 and 16 to get the usual Hanle signal. From the FWHM of the curve, calculate the lifetime of the level from eqn 1.1.

2.6) Applications of the zero field level crossing

In the following section, I will review briefly some of the most important applications of zero field level crossing and in particular the Hanle effect. A more detailed review can be found in references [16,7, 3].

1) Life-time measurements

Because of its inherent simplicity, the life-time as measured by the Hanle effect has a degree of accuracy which compares favourably with other techniques. The typical uncertainty is 3-4%. This level of accuracy

is only possible without line-broadening sources (such as stray magnetic field, Holtzmark effect and power broadening and line-narrowing process such as coherent diffusion) so that the experimentally recorded line width practically coincides with the natural width. In this case the life time τ of the level can be obtained from eqn (1.1).

The transverse Doppler effect will only affect the intensity of the fluorescent signal and will not broaden the width of the Hanle curve.2)

2) Magnetometry

From the measurements of the width of the Hanle curve (ΔB) one can determine the product $g_J \tau$ (see eqn (1.1)). So conversely if g_J and τ and the shape of the level crossing curve are known, the Hanle effect can be used to determine the strength of the external magnetic field.

3) Laser cooling of atoms.

There is a variety of methods for the cooling of the atoms by optical means. Coherent Population Trapping (CPT) provides the basis for one of the techniques in which ultra-cooling of the atoms can be achieved (Temperatures on the order of 10^{-6} K can be reached) [11].

The technique was first used by Aspect et al in 1988 to cool metastable helium atoms [37]. A description of the laser cooling of atoms by CPT is given by I.E. Mazets et al [38]. In CPT the ground state sub- levels of the atom are trapped in a coherent superposition for which the fluorescence

signal ceases at zero velocity. Atoms with other velocity distributions (a Doppler shift is always present) scatter photons in random directions, and in the course of a random walk in momentum space these atoms will be finally trapped in the non-absorbing state. As time elapses, they accumulate there.

Chapter 3

Optogalvanic spectroscopy

3.1) Introduction

In this chapter, I will review the basic properties of optogalvanic (OPG) spectroscopy which was used to calibrate the diode laser wavelength.

The OPG effect was first discovered by Penning in 1928, who reported a variation in the impedance of a neon discharge when it was subjected to the irradiation from another neon discharge [39].

However, the interpretation of the OPG effect requires a model which often involves the description of the discharge itself. The full description of the discharge requires knowledge of the electron energy distribution function. The parameters which characterise this function are:

i) The elementary processes and atomic states to be considered

ii) The number density of the ions

iii) The population density of the atomic states involved in the ionisation.

The task is so difficult that experts usually view the progress of any discharge modelling along with the progress in specification of the above parameters.

In this work, we will only look at the contribution of the various ionisation processes to the OPG effect and the polarity of the signals. We do not consider the equations which describe the change in number density of the ions, metastable atoms and electrons etc. The sign of the signal can be positive or negative depending on the position of the irradiated discharge volume, the discharge current and the atomic transition [40]. In general, the explanation about the signal polarity is centred around two proposals: [41,42]

1) Laser excitation of atoms from a level with a small ionisation probability to the levels which have a large probability of ionisation in the discharge leads to an increase in electron impact ionisation. This increase in the ionisation cross section results in more excited atoms becoming ionised and so the conductivity of the discharge increases. Alternatively, if the laser excites atoms from a level with a large probability of ionisation to a level with a small probability of ionisation, the conductivity of the discharge decreases [41]. The polarity of the signals is defined as negative when the conductivity of the discharge increases and vice versa.

2) Laser excitation perturbs the equilibrium established between the electron temperature and the atomic excitation temperature. However numerous elastic and super elastic collisions between the electrons and the excited atoms restore the equilibrium, with the excess of energy transferred to the electrons. This excess of energy shifts the electron energy distribution in the discharge to a higher level and hence the conductivity of the discharge increases [42].

It is evident that these two suggestions can not be brought easily into a model capable of predicting the sign of the OPG effect.
Nevertheless, interest in OPG spectroscopy and its related phenomena has grown steadily in recent years with the increasing variety of lasers. OPG spectroscopy has a large range of applications.

The technique has been extensively applied to the study of the refractory metals. The vapour of these metals can be produced by sputtering of the cathode materials by the ions of the carrier gas [43]. The OPG effect can provide a reliable method to calibrate the wavelength of tuneable lasers for most spectral lines. The OPG atlases of many transition lines of the atoms are available and are upgraded continuously. The OPG method can be used to determine the laser bandwidth [44]. It might also be applied to detect the non-linear Hanle effect [45]. The other important applications of OPG are the stabilisation of the laser frequency [46], analytical chemistry and flame spectroscopy[47].

The most important advantages of the OPG spectroscopy are: high sensitivity and very simple set up. The principle disadvantage is in the fact that the useful regime of the discharge is limited to a narrow range of discharge parameters. It might be difficult, for example, to detect a signal at a particular value of the current, gas pressure or even the position of the discharge with respect to the laser beam.

In general, the OPG techniques for detection of the transition lines of the refractory metals and the noble gases and laser wavelength calibration perform almost the same as traditional grating techniques, with the real advantage of inherent simplicity [48].

3.2) Basic properties of a dc discharge

The basic properties of electrical discharge are usually understood in terms of regions with specific values of current and voltage. A typical current- voltage characteristic for a low pressure glow discharge is shown in fig 3.1. Of all the different regions in figure 3.1, the glow discharge is the best understood. The glow discharge is divided into 3 sub-regions: namely, normal glow, the subnormal glow and the abnormal glow. In the normal glow region, the voltage remains constant over a wide range of currents. The cross section area of the glow expands with current until it covers the entire cathode. In the abnormal glow region an increase in the current would result in a sharp increase in the voltage. In contrast, the subnormal region is where the voltage drops sharply as the current increases [49].

Glow discharges have a variety of different shapes depending on: the geometry of the electrodes, the distance between electrodes and their material type, the pressure of the sustaining gas and the dimensions of the containing glass [50].

In general, for a cylindrical tube with a flat cathode, there are alternate dark and bright zones as it can be seen in the figure 3.2. The generation of these different zones can be explained as follows [51]. In an enclosed glow discharge tube, there exists a noble gas and positive and negative electrodes. A potential difference smaller than the electrical breakdown critical value of the gas causes very little flow of the current density along the lines of force of the electric field.

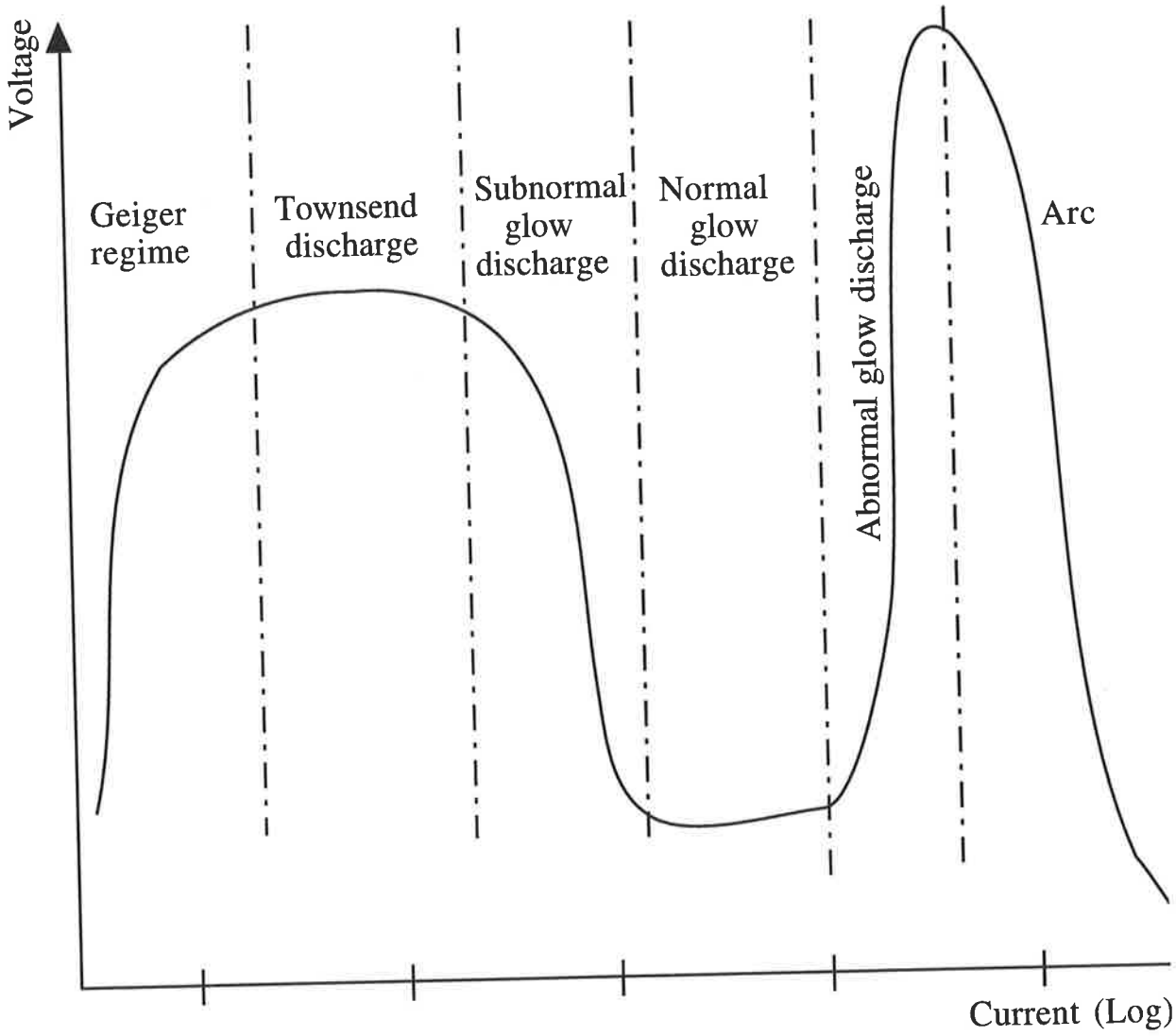

Fig 3.1: V-I characteristic of discharge between electrodes for a wide range of currents for a flat cathode discharge[51].

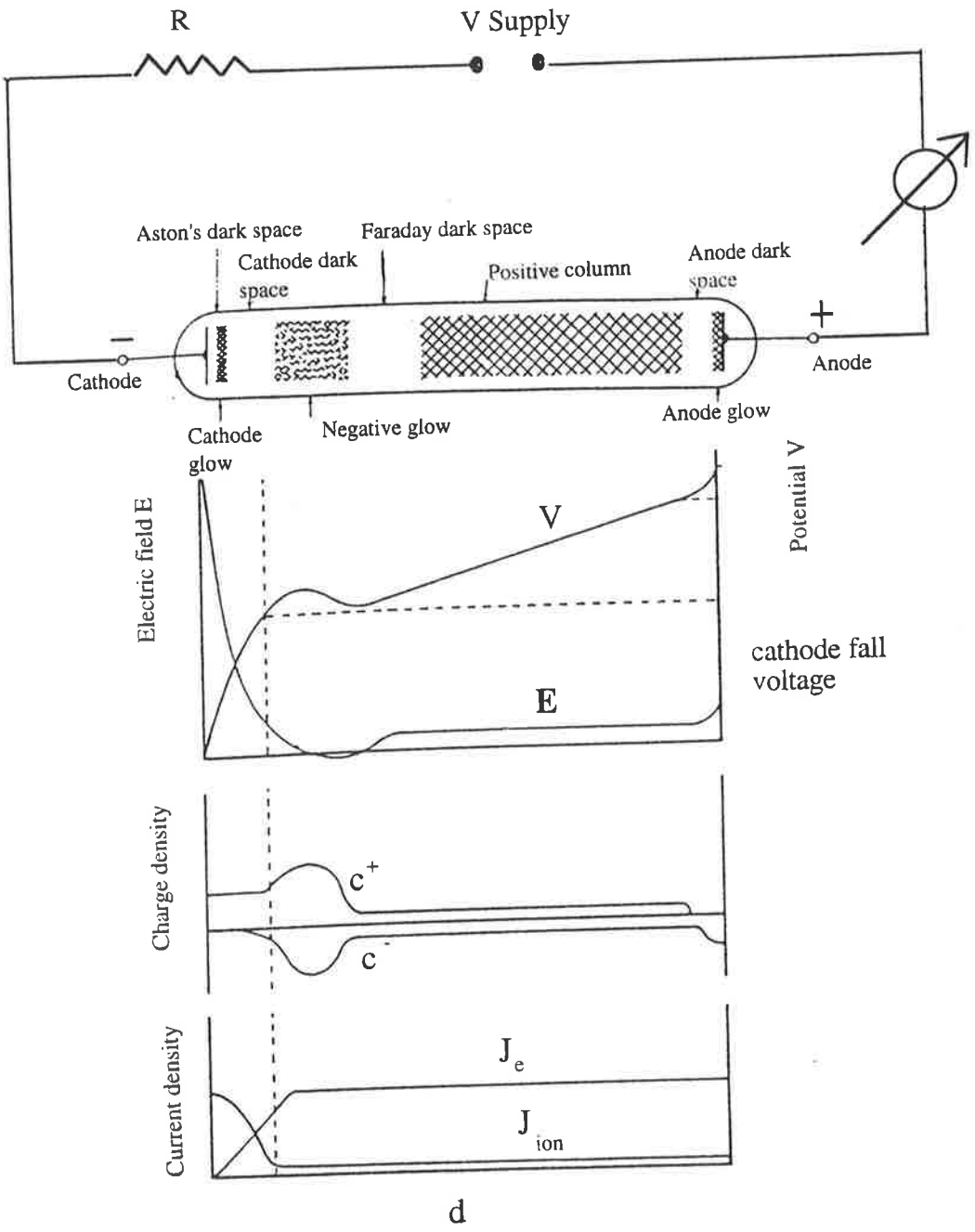

Fig 3.2. : Spatial distribution of dark and luminous zones, electric field **E**, Potential V, Space charge densities c^+ and c^-, electron and ion current densities J_e and J_{ion} [52].

If, however, the potential difference exceeds the critical value of the gas electrical breakdown, then the gas abruptly becomes a conductor. A sufficiently large electric field and the existence of some initial free electrons in the container are two necessary conditions for the breakdown process to occur. These initial electrons usually exist in any sample of gas under normal conditions by the action of some external influence such as cosmic rays [51].

Primary electrons that cause a self-sustaining discharge are produced from the ionisation collision of the initial free electrons with the gas. The secondary electrons separate from the cathode by the bombardment of positive ions and to a lesser extent by the photoelectric effect. As shown in figure 3.2, in the *Aston dark space* the secondary electrons have not travelled far enough from the cathode to acquire enough energy and thereby to excite the atoms of the gas. The next region is a thin glow region in which electrons move sufficiently in the cathode electric field to gain energy corresponding to the threshold of the excitation energy. This region is called the *cathode glow*. The next region is *the cathode dark space (Crookes dark space)*, characterised by the presence of high energy electrons. These electrons induce ionisation with high probability and so result in a strong electron multiplication with the new born electrons having smaller excitation energy [53]. In this region a large positive space charge builds up and the current transfers mostly by ions. The potential across the cathode dark space is known as the cathode fall voltage and is approximately equal to the applied voltage. The next zone is known as *negative glow*. In this region , the large numbers of secondary electrons begin to excite the gas atoms. This results in a strong emission of light. The emitted light contains many spectral lines . The order of appearances of the spectral lines obey Seeliger's rule. According to this rule, the negative glow first reveals the lines that are emitted from

higher atomic levels and then lines from lower levels as electron energy falls with increasing distance from the cathode. In the negative glow the electric field reaches a minimum.

The small value of the electric field promotes the recombination between electrons and the ions. The luminosity of the cathode glow decreases toward the anode as it merges into another dark space called the *Faraday dark space*. In this region the electrons decelerate and suffer considerable energy loss. The Faraday dark space is characterised by the presence of ground state particles and despite the fact that the electrons in this region have decelerated considerably and may even encounter a retarding field on their route toward the anode, their strong concentration gradient and large electron temperature combine to cause them to diffuse forward toward the anode. The *positive column* is the region of zero axial gradient of ion concentration. The motion of electrons in the positive column is no longer beam like, as in the negative glow, but essentially random (i.e. the electric current in this zone, as in the Faraday dark space, is essentially due to diffusion). In proximity to the anode, a negative charge region is formed by the electron attraction. Thus the electric field increases again and the electrons accelerate. The accelerated electrons form an *anode glow* right in front of the anode [54].

An increase of pressure results in a compression of the cathode dark space, negative glow and Faraday dark space which contract toward the cathode. A decrease of the distance between the cathode and anode produces a shortening of the anode glow [50]. When the anode is placed near the cathode edge of the negative glow, the voltage necessary to sustain the discharge rises rapidly and the discharge is said to be obstructed.

In an obstructed glow discharge, the positive column is absent . This shows the positive column is not essential for maintaining the low pressure glow discharges.

If, however, the cathode is formed by two flat electrodes, or a hollow cylinder tube, then the intensity of negative glow increases considerably. This is called a hollow cathode discharge and will be discussed in the next section.

3.3) Hollow cathode discharges

In a hollow form of the cathode, the negative glow will flow into the cathode at an appropriate pressure due to the field gradient around it. With a suitably placed anode and proper electrode arrangements, the light emitted is completely of the negative glow type, and consists of very sharp spectral lines of the discharge gas and the cathode metal [55]. The spectral lines of the cathode metal are present in the discharge because of the sputtering of its surface by the carrier gas ions. The sputtered materials give rise to an atomic vapour that finally condenses on the wall of the glass tube. (see fig 3.3)

The electrode arrangements which support the formation of hollow cathode discharges usually use a cylindrical type of cathode open at least at one end and with an anode in the form of a ring placed near the open end. A second anode ring encircling the body of the cathode or placed along the cathode may also be used [56]. This allow part of the negative glow to form over the outer cathode surface. The Sm-Neon hollow cathode discharge is shown in figure 3.3.

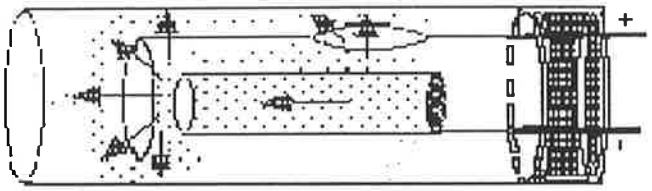

Fig 3.3: Schematic diagram of a Sm-Ne hollow cathode discharge. The diagram also illustrates the manner in which the sputtered Sm atoms from the cathode are distributed in the tube [57].

This design allows the discharge to handle larger currents compared to a flat cathode discharge. Another property of a hollow cathode discharge is the existence of a strong electric field in the cathode dark region which accelerates ions more strongly than normal plane glow discharges. This higher acceleration rate causes very effective sputtering of the cathode metal.

The hollow form of the cathode also significantly increases the chance of both positive ions and photons to hit the cathode surface. This will increase the sputtering of the cathode material by a large amount . Another important property of the hollow cathode lamps is their stability for long hours of working [50].

The length of positive column is shortened considerably in the hollow cathode discharge (i.e. an obstructed type discharge) and so the fast electrons from the cathode dark space travel mainly in the Faraday dark space. Some of these electrons will however have their motion retarded and return to the glow possibly due to the field effects of the opposite wall of the cathode or by random motion in the near zero field which exists in the beginning of the Faraday dark space [31a,56]. Therefore, a number of electrons can make double or multiple passages within the cathode hole, producing, as compared with a plane cathode discharge, a greatly increased number of ions and photons. Hence both the current and intensity of the emitted discharge are further increased.

There is a possibility of quenching certain transition lines in the hollow cathode due to some unknown processes [56]. However for Samarium the data is insufficient for any conclusion to be made about the possible quenching of some lines in the Sm-Ne hollow cathode discharge.

The effect of the magnetic field on the hollow cathode discharge was discussed by C.Poporici [58]. He found the presence of a magnetic field in a glow discharge is equivalent to an apparent increase in discharge pressure given by

$$\frac{\Delta P}{P} = 9.5\times10^{-3}\frac{\eta^2}{m_e T_e}(\frac{B}{p_o})^2,$$

where P is the gas pressure in mmHg, B is the magnetic field (Oe), T_e is the electron temperature (K), m_e is the electron mass (amu) and η is the mean free path (cm) at 1mmHg. Therefore the use of the Hollow cathode discharge in the presence of the magnetic field enhances the probability of detecting very weak transitions at very low gas pressures.

Under certain experimental conditions, OPG can be also used to determine the linewidth of the excitation laser. A list of these conditions for the hollow cathode discharges is given by E. M. Van Veldhuizen et al and listed here [40]. The first condition to be considered is that the laser intensity should be small relative to its saturating value. The lower level of the transition should not be metastable or a resonant state near a metastable. Another condition is that the laser beam should only be weakly absorbed by the discharge; i.e. the discharge current should be as low as possible. The final condition is that when measuring the effect with lock-in techniques (see chapter 4 figure 4.9), the chopping frequency should be low in order to obtain a real steady-state situation. Fulfilment of these conditions reduces the width of the transition to its Doppler width. When the bandwidth of the laser is much broader than the Doppler

width of the transition, then the recorded width of the transition directly gives the laser line width.

3.4) Sm -Neon discharge mechanism

In this section, I describe the general modelling of the hollow cathode Sm-Neon discharge. The parameters of this discharge have not been calculated yet, therefore we only evaluated the contributions of the various ionisation processes in a qualitative manner. The transitions that have been studied in this thesis are the ones to which we had access with our diode laser. They are indicated in the partial energy diagram of neon and Sm as shown in figure 3.4 and 3.5.

We used a 5-level scheme developed by E.M. Veldhuism to explain the polarity [59]. The model only predicts the polarity of the signals related to the discharge current and the transition type of Ne. Within the accessible range of our diode laser, there are only two neon transitions $1s_2 \rightarrow 2p_4$ at 667.8 nm and $1s_2 \rightarrow 2p_5$ at 671.7 nm.

The foundation of the model is described in figure 3.6 [59].
In this figure, G is the ground state, + is the ion state, M is a metastable level, 1 is a resonance, a metastable or highly excited level and 2 is a highly excited level. In this model the laser coupling is always between levels1,2 (which is indicated in the figure by red arrows). The solid black arrows indicate ionisation and de ionisation process in the absence of irradiation. The blue arrow shows the direction of the radiation-induced changes in the rates of the process.

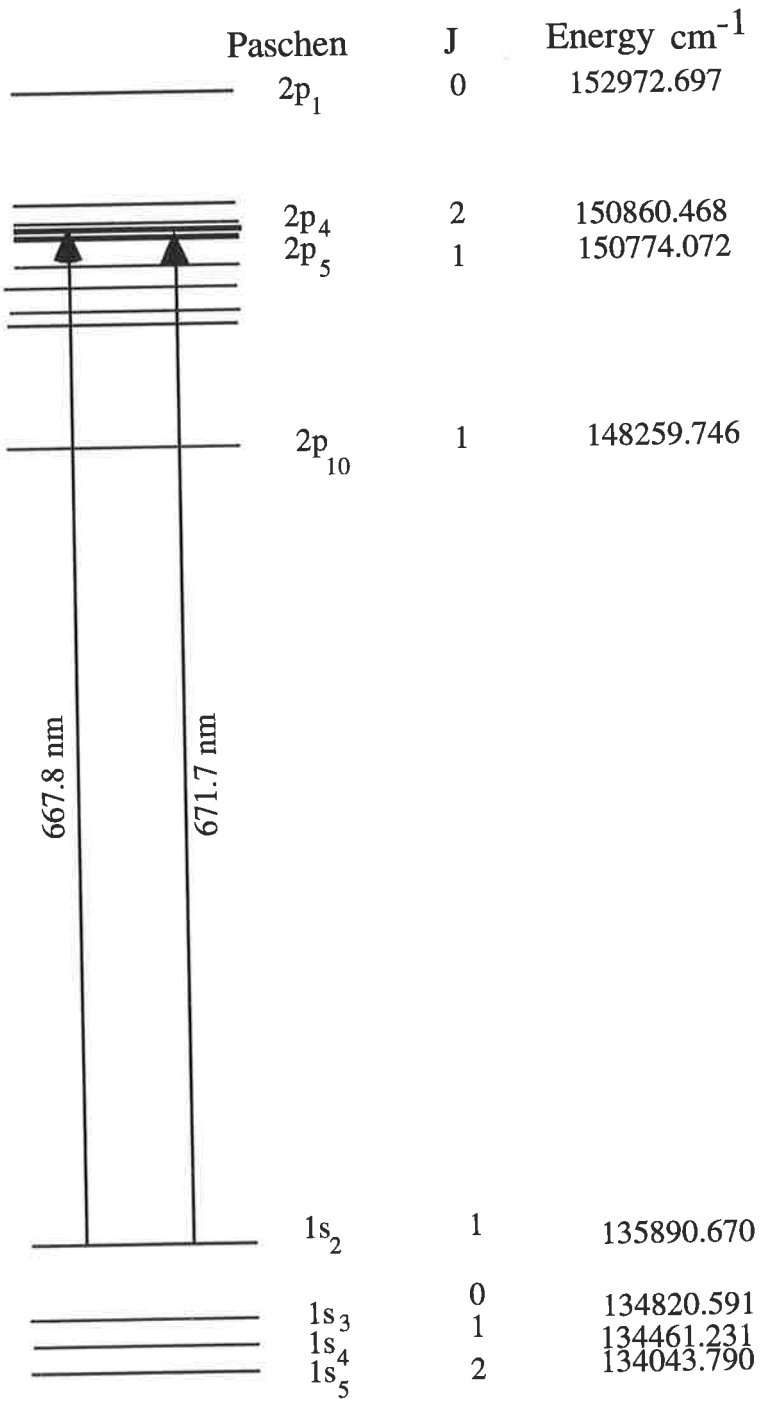

Fig 3.4: Partial energy- level diagram of the first and second excited states of Neon. The two transitions in the accessible range of the diode laser are shown.

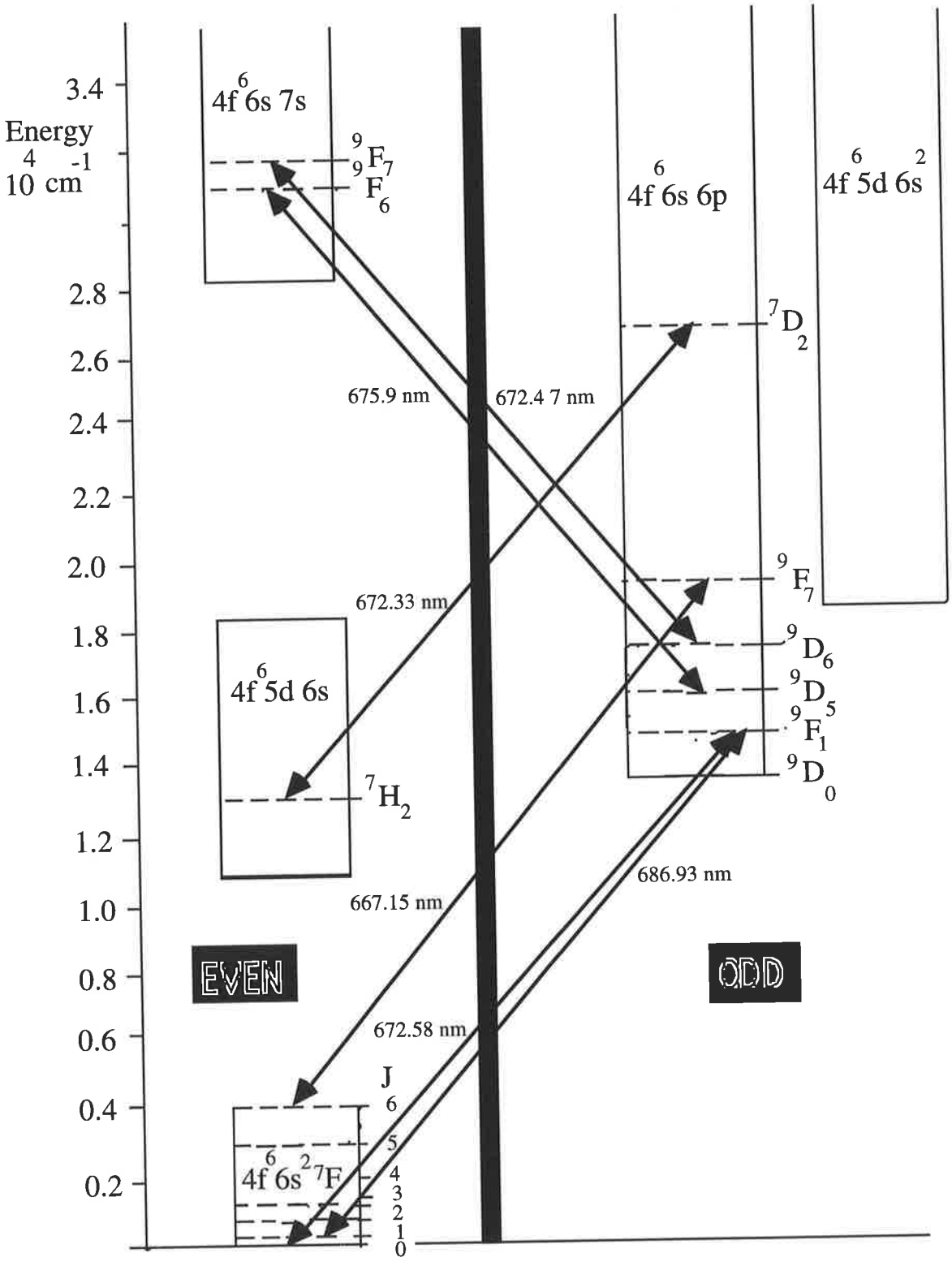

Fig 3.5: Partial energy level diagram of SmI, including the levels and transitions of SmI which lies in the accessible range of the laser (without external cavity). Designation of the levels are taken from reference [61] while the transitions are taken from reference [62].

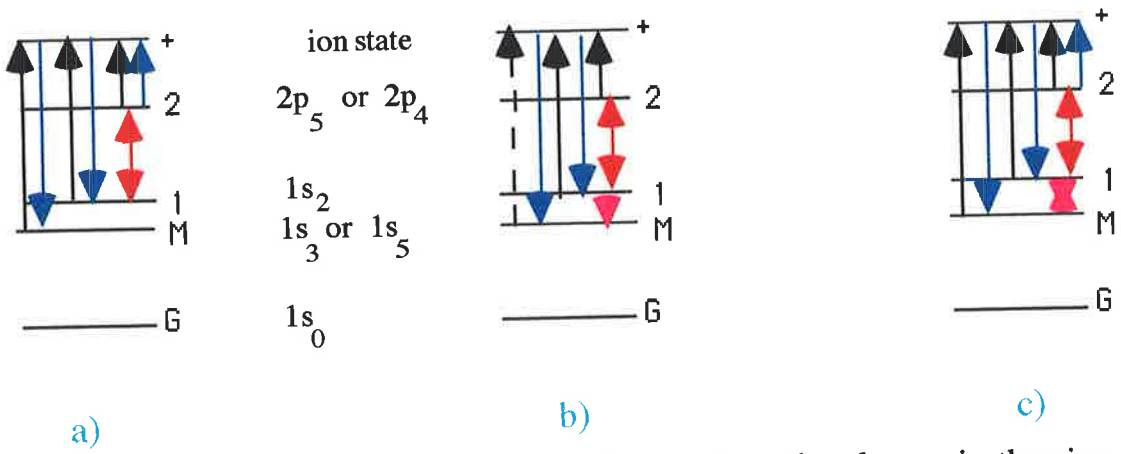

Fig 3.6: Diagram of the five-level model to explain the change in the sign of OPG related to discharge current. The solid black arrows indicate ionisation and de ionisation process in the absence of irradiation. The red arrows show the laser coupling between levels 1 and 2. The blue arrow indicates the direction of radiation-induced changes in the rates of the process. The pink arrow indicates the coupling between 1 and M.

case a) **The transition 1-2, weak discharge current.** The electron density is low and does not allow for a coupling between 1 and M. The population of 2 increases by laser excitation from 1. The radiation emitted from the higher excited state 2 will lead to ionisation by photoionization . As a result the conductivity of the discharge increases, i.e. the signal is negative.

case b) **The transition 1-2, medium discharge current.** The current density is high enough for mixture of 1 and M which results in the decrease of the metastable density upon optical pumping of level 1 population into the level 2. The decrease in the metastable density causes the weakening of the ionisation as we have less frequent collisional ionisation process between metastables . The current density is however too low to produce an significant collisional ionisation from level 2. Therefore, the enhanced ionisation from level 2 does not compesonate the loss of ionisation from the metastable level. Therefore the signal is positive due to decrease in total ionisation rate in the discharge.

case c) **The transition 1-2, High current**. The metastable level M and level 1 will be coupled together . The population of M is saturated at such high current density. The population of 2 will however continue to rise by laser excitation from level 1. As a result the net rate of ionisation increases in the discharge. The signal polarity is negative.

The transitions at the wavelengths corresponding to the transitions of the sputtered Samarium species would result in increased populations of excited states. These states are then ionised by collisions with electrons or with metastable Neon gas atoms. This will increase the conductivity of the discharge and negative polarity signals can be expected for all these transitions. As figure 4.9 shows, we detect the voltage change across the Ballast resistor. The negative voltage change corresponds to a current increase and a positive voltage change to a current decrease.

CHAPTER 4

Setting up the apparatus, Experimental procedure and results

4.1) Introduction

The project involved the design and construction of the apparatus as well as optogalvanic spectroscopy of some Sm and Ne levels in the tuning range of our diode laser. This chapter includes the details of the experimental apparatus, set up, procedure and a discussion of the results of the optogalvanic spectroscopy.

In section 4.2.1 we discuss the vacuum system and magnetic field generation.

Section 4.2.2 contains a discussion of the oven and the atomic beam collimation. We also found the lifetime of the excited state $^9F_1$ of Sm based on the available data on oscillator strength and branching ratio.

Section 4.2.3 is devoted to the diode laser and the construction of its accessories. The circuit of the laser diode temperature controller is discussed in this section.

Section 4.3 discusses the experimental technique for the detection of the OPG signals. The OPG technique is used to calibrate the wavelength and bandwidth of the diode laser.

Section 4.4 considers the results of the OPG spectroscopy and its analysis.

Section 4.5 contains the conclusion.

4.2) Design and construction of the apparatus

4.2.1) The vacuum system and the magnetic coils

The vacuum system consists of 2 differentially pumped chambers, an oven chamber, and an interaction chamber, and is schematically presented in figure 4.1. The pressure in each of the chambers was monitored independently with two Bayard-Alpert gauge heads and a Philips 307 vacuum gauge controller. The typical background pressure which was observed in the chamber after 24 hours pumping was of the order of 1.2×10^{-7} Torr, although it must be noted that a pressure of 5×10^{-8} Torr will be reached after 3 days.

The design of the vacuum system was based on two criteria in order to make sure that the optimum condition in detecting the signal will be achieved. The first criterion was the type of the material used in the construction of the vacuum system. The second criterion was the length of the atomic beam in the oven and scattering chambers. The materials used in the construction of the vacuum chamber were non magnetic stainless steel and bakeable. The reason for the use of non-magnetic materials was to reduce the effects of the laboratory stray magnetic fields (see section 2.3). The length of the atomic beam in the oven and scattering chambers should be as short as possible to increase the density of the atomic beam in the scattering chamber [63]. However, due to the

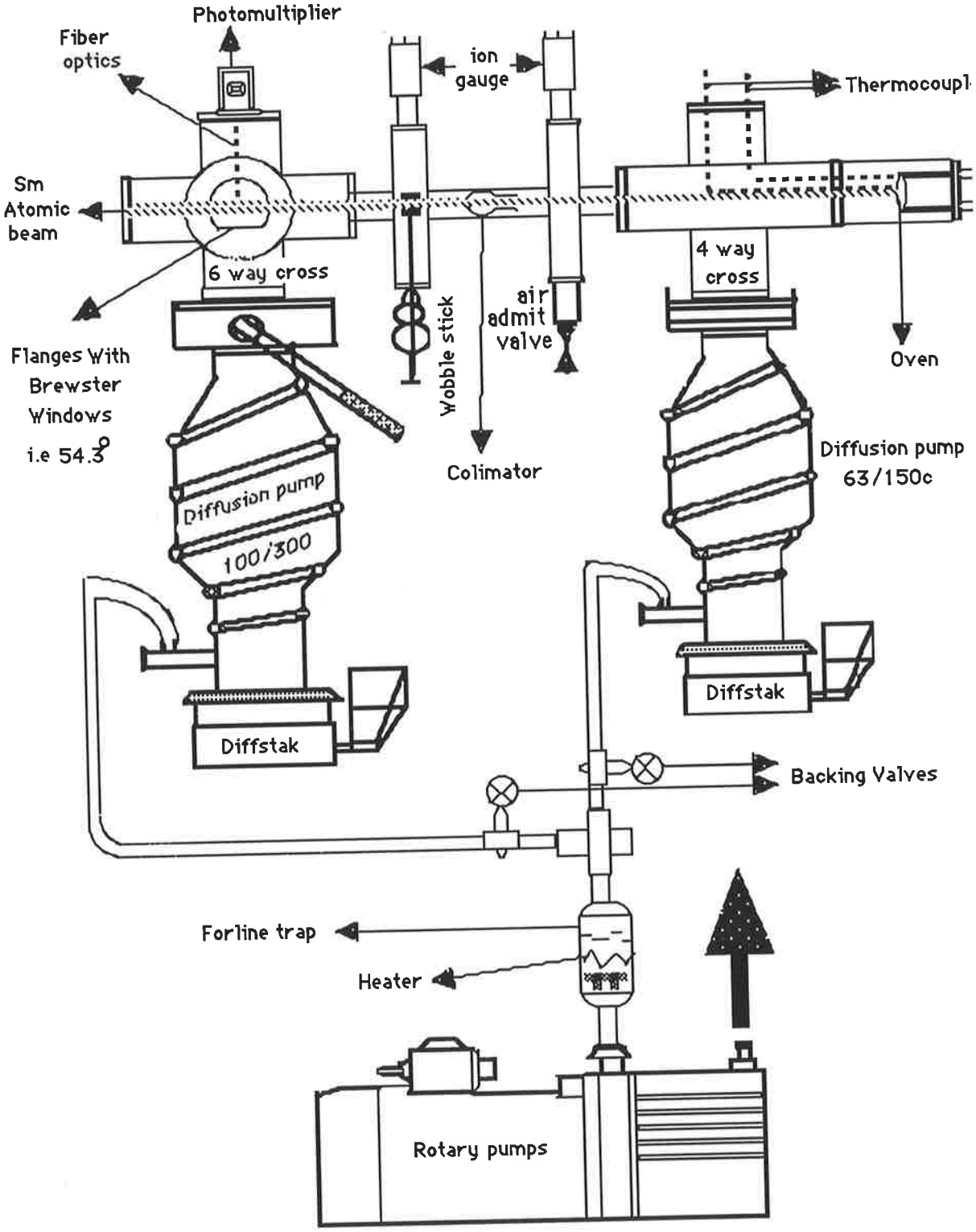

Fig 4.1: Diagram of the vacuum chamber

presence of the induced magnetic field of the oven, we moved the oven further away from the interaction region. The oven also needs to be a reasonable distance away for good beam collimation. As a result the total length of the beam from the oven chamber to the scattering chamber was 87 cm. A 1.1mm collimating hole was placed 58 cm from the oven chamber. The source chamber, was a four way cross with an arm containing the oven and another arm allowing the exit of the 2 thermocouples.

The interaction chamber contained the fiber bundle to transfer the emitted fluorescence light to a R928 photomultiplier outside the chamber. Two Brewster angle windows were placed at the end of two arms to avoid the reflection of excitation laser light from entrance and exit windows. The windows were 6mm thick, of BK7 glass and were attached to the vacuum flange by a low pressure epoxy (Torr Seal by Varian). The wobble stick will be used for the detection of the Sm beam.

Around the interaction chamber there are two mutually perpendicular sets of square Helmholtz coils and a pair of circular main coils. These three pairs of coils are perpendicular to each other. The position of the oven, Brewster angle windows and coils correspond to the geometry of figure 2.2 in chapter 2. The Helmholtz coils are used to annul the vertical and horizontal earth's magnetic field (locally, 500 mGauss vertical, 220 mGauss horizontal). The vertical component of the earth's magnetic field is reduced to about 1.5 mGauss by the pair of a square coils of length 60 cm and the horizontal component of the field is reduced to 2 mGauss by the pair of square Helmholtz coils of length 50 cm. The distance between Helmholtz pairs were near to Helmholtz spacing to achieve the maximum volume field uniformity. The Helmholtz spacing for square coils is 0.5445 times the length of a side[64].

The main coil which produces the applied magnetic field was designed to achieve a field uniformity better than 1 percent on the interaction volume of 2 cm^3 . Since for the $^9F_1$ level with a lifetime of $(1.17 \pm 0.23) \times 10^{-6} s$(i.e. Larmor frequency $\omega_l = (9.0 \pm 0.4) \times 10^6 s^{-1}$) such a field uniformity would broaden the HWFM of the signal by approximately 1 mGauss which corresponds to an error less than 1 percent in the measured lifetime.

At 16.7 gauss, the field uniformity was measured to be $(5 \pm 1) \times 10^{-3}$ over the interaction volume. It was measured with a Bell model 640 Gauss meter. The magnetic probe was positioned in the centre and in different places of the interaction region (such as the boundary of the region). At each point , the value of the magnetic field is measured many times. The mean and standard deviation of each set of data was calculated and a t-test was performed to decided whether the field at the centre and the other measured points have the same mean at 5% significance .

The main coil had 137 turn enamelled copper wire number 12 gauge in a 10 cm diameter. At 6 Amperes, the magnetic field produced by the coil was 30 gauss. The currents for the coils were provided by two power supplies Goodwill model GPC 3030D.

4.2.2) Construction of the oven

A tubular type oven was used to produce the Sm atomic beam. A schematic diagram of the oven is shown in figure 4.2.

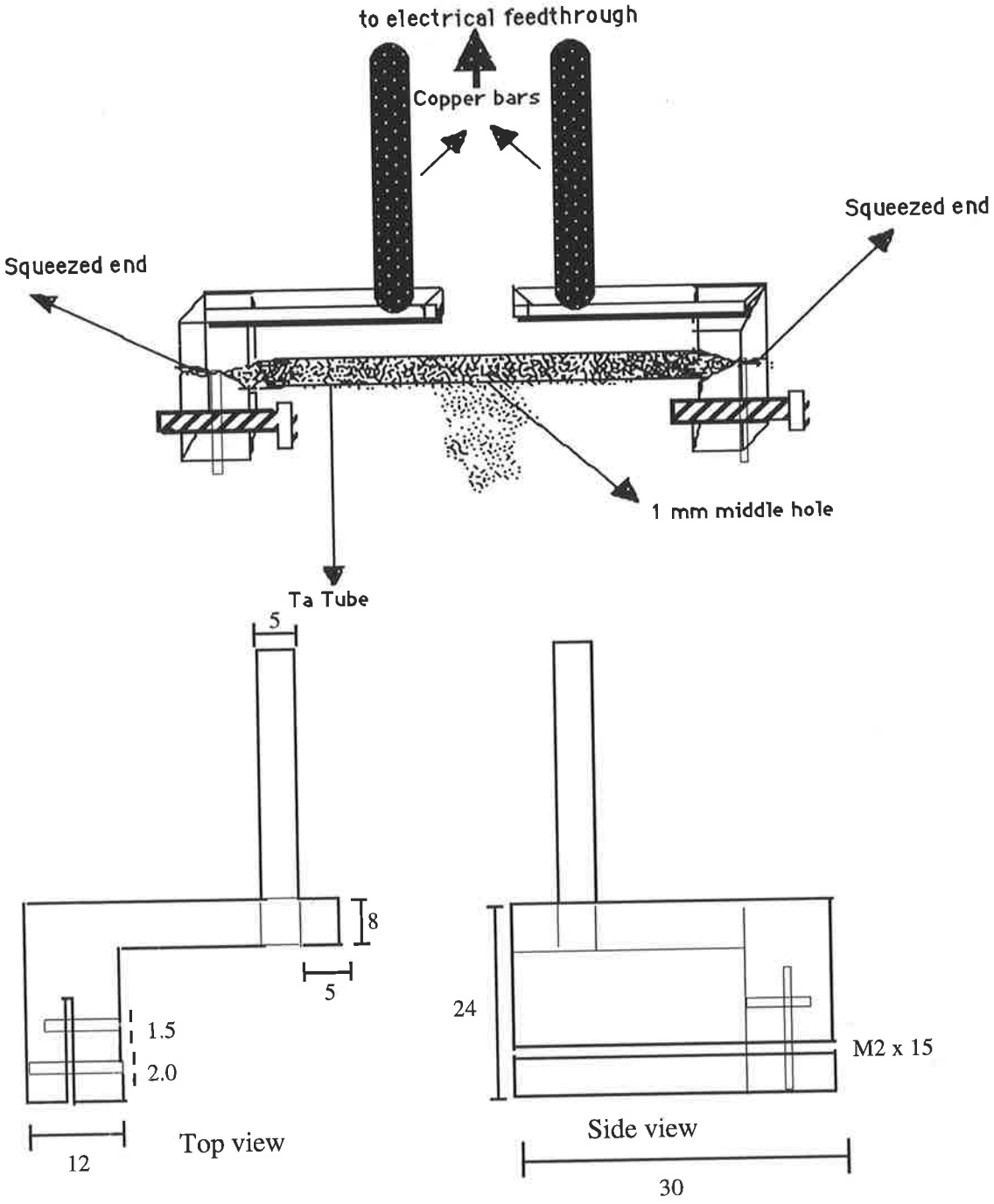

Fig 4.2: diagram of the oven and mechanical drawing

The main body of the oven is a Tantalum tube with width 8.7mm ,length 50 mm and thickness 0.08mm. Tantalum is used since it does not react with Sm and its melting point is well above that for Sm (2996^{o} C for Ta compared to 1073^{o} C for Sm). The end of the tube was clamped by a

stainless steel block. The ends connected directly to the secondary coil of a DC transformer. A small circular hole of diameter 1mm was drilled in the middle of the oven to allow the exit of evaporated Sm. The oven temperature was measured using two type N thermocouples. One measured the temperature of the cooler end of the tube, the other monitored the hotter part of the tube right over the exit hole. The thermocouples were calibrated by comparing them with a calibrated reference thermometer model 362 Pyrometer made by Pitman Ltd. The method of the thermocouple calibration is shown in figure 4.3. A routine check on the calibration characteristics of the thermocouples is recommended. The reason is that the calibration of the thermocouple over some reasonable time changes due to the vaporisation of Chromium in the positive element in the vacuum [65].

The temperatures from the cooler and hotter parts of the oven differ considerably. I noted a temperature difference of about 200^{o}C between the central hot part and cooler ends. The centre hole was at the hottest point in order that no Sm could condense in the centre exit hole. The temperature of the oven reached 660^{o}C at 150 W power (vapour pressure is 10^{-3} Torr at this temperature). The current through the oven was 130 A.

To prevent the melted Sm from conducting the current, a boat made of Tantalum was made to contain the Samarium samples.

We also present a new method for the detection of the Sm atomic beam in appendix 3. The basis of the method is the reflection of a nanosecond pulse by a coil whose core contains the deposited Sm on a insulator.

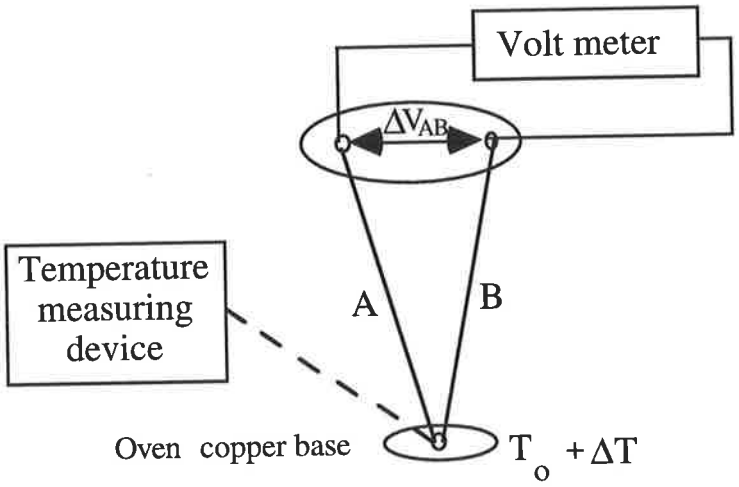

Fig 4.3: Schematic arrangement for the relative calibration of the thermocouple. T0 is the temperature of the oven when it was turned off. T0+ΔT is the reading of the reference thermocouple . For each selected calibration point ΔT, the measured emf of the tested thermocouples is ΔV_{AB}. The graph of ΔV_{AB} versus ΔT yields a proportionality constant which can be used to calibrate the thermocouple .
The measuring junctions of the test and reference thermocouples are always maintained at the same temperature, by wrapping them together and then putting them in a screwed hole which drilled in the copper base of the oven [65].

The average velocity of the Sm atomic beam is about 430 m/s for the oven temperature 660°C. The angular divergence of our oven beam is θ=o.o2 rad (see figure 4.4). Therefore from equation 2.12 one obtains for the present system a transverse Doppler width of about $\Delta\nu_D$=13 MHz for 672.58 nm transition line of Sm.

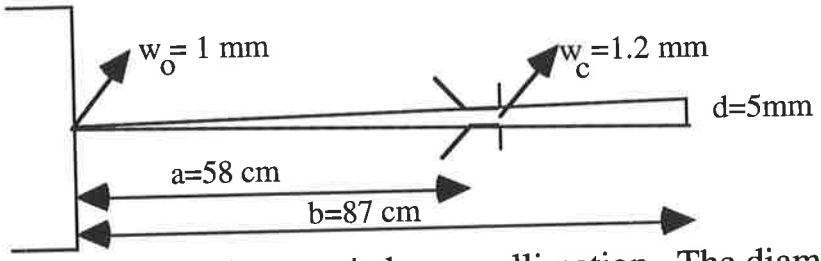

Fig 4.4: Geometry of the Sm atomic beam collimation. The diameter d of the beam at the interaction region can be found from:

$$d = |w_C + (w_C + w_O)\frac{l_t}{l_o}|$$

where W_O is diameter of the oven aperture, W_C is the diameter of the collimator aperture, l_t is the total length of the beam and l_o is the length of the beam in the oven chamber [66].

As we discussed in section 2.4, theoretically the transverse Doppler spread should be smaller than the natural linewidth. The natural linewidth can be found from the equation 2.13. We calculated the life time of the $^9F_1$ level by the *branching ratio* method [67]. To find the lifetime of an excited state level by the branching ratio method, we followed the following procedures:

1) Firstly, we found all possible emission lines which originated from a common atomic level. In atomic physics, these groups of emission lines are known as "branches".

2) we obtained relative transition probabilities for each branch by using [68]:

$$A_{ij} = (\frac{8\pi^2 e^2}{m_e c})\frac{g_1}{g_2}\frac{f_{ij}}{\lambda^2}$$

Where A_{ij} is the transition probability of level i to decay to level j, g_1 and g_2 are the statistical weight of the level, f_{ij} is relative oscillator strength of the transition, e is the charge of electron and m_e is the electron mass.

Thirdly, we found the life time τ of the level i by summing the transition probability of the individual branches; i.e.

$$\tau = \frac{1}{\sum_i A_{ij}}$$

The $^9F_1$ level has 2 branches:

It can decay to the ground level $^7F_0$ by emission of light of wavelength 672.58 nm, and to $^7F_1$ level with the emission of light with wavelength 686.6 nm. The oscillator strength for the two levels was found from Komarovskii et al [69]. We used the conversion factor, $(18 \pm 1) \times 10^{-5}$, determined by Blagoev et al to put the f values on an absolute scale [70]. Blagoev et al calculated the conversion coefficient from the relative values of the oscillator strength in reference [69].

The lifetime of the level $^9F_1$ is calculated to be $\tau_{9_{F_1}} = 1.17 \pm 0.23$ μs.

Where the uncertainty in the derived lifetime was estimated to be 20% [71]. However additional uncertainty may exist due to the unknown branches in the summation of the transition probabilities.

Therefore the natural line width of the level is about 0.14 MHz .

The line width due to the power broadening is 0.38 MHz at 3.8 mW laser power. From these considerations, it is clear the main source of the line broadening is the Doppler effect.

The geometry of the system also determines the degree of the focusing of the laser beam. Since the diameter of the atomic beam is 5mm in the interaction region, the diameter of the laser beam should be 5mm minimum. For the laser focus of 5mm the transit line width is small. Transit line broadening occurs when the flight time of the atoms through the laser beam is shorter (or in the same order) than natural lifetime of the atoms [33].

4.2.3) Diode laser and the construction of the temperature controller

In this section we will consider the diode laser characteristics which are used throughout the experiment.

The laser is a 670 nm *TOLD9211* from Toshiba. It is an index guided 5mW laser. As the temperature of the diode laser rises, the number of modes in the cavity rises. The number of modes also changes as the injection current changes. We observed these changes in the number of laser modes using a grating spectroscope. Typical separation between modes is 160 GHz which corresponds to a 300 μm resonator length. All signals detected by OPG spectroscopy had similar HWFM. However we can not conclusively deduce that the HWFM of the signals are due to the Laser bandwidth. The reason being that the laser beam intensity was very close to the saturation level and different transitions may have similar HWFM under the condition of saturation.

I calculated the minimum linewidth of the free running laser from the modified Schalow-Townes formula:[72]

$$\Delta\upsilon_{FWHM} = (h\upsilon_L/8\pi P)L^{-2}\ln(R)[\ln(R) - aL]v_g^2 n_{sp}(1+\xi)$$

Where υ_L= frequency of the diode laser

P= Output power of the diode laser (**3.5 mW**) ,

L= Laser cavity length (**0.3 mm**), R= mirror reflectivity(**0.3**),
a= Loss coefficient (**4500 cm^{-1}**), v_g= group velocity (**7.52**$\times 10^9$ **cms^{-1}**),

n_{sp}= The spontantaneous emission factor (**1**) and finally ξ= **3.5** is the ratio of the real to the imaginary part of the refractive index

The minimum linewidth of the free running Diode laser is calculated to be 9MHZ. In my calculation, I didn't consider the increases in the linewidth due to fluctuations in the carriers, the temperature and in the

susceptibility of the laser. As a result the true linewidth could be higher by a factor of 2 or 3. Also the diode laser linewidth increases as the temperature decreases. However, at the present time the mechanism for this temperature dependence is not clear [73].

The diode laser had an asymmetric divergence of $\beta_{\parallel} = 8^{o}$ and $\beta_{\perp} = 31^{o}$ which produced a laser beam with elliptical cross section .

The output power and its wavelength depends on both the diode junction temperature and injection current. Therefore stable laser operation requires that these quantities be precisely controlled [72]. The laser wavelength changes with temperature as both the optical length of the cavity and the gain coefficient depend on temperature. However, the rate at which the optical length of the cavity changes with temperature is different from the rate of change of the gain coefficient (and hence the gain curve shifts). This results in a temperature tuning curve which has a staircase appearance with sloping steps (see fig 4.5). The slope of each step is due the tuning of the cavity mode while the jumps between steps correspond to hopping from one mode to the next . We did not measure the slope of each step. Sometimes the wavelength corresponding to a given transition occurs exactly at the value in which the laser jumps from one mode to another and so the laser will miss (or pass) the transition. The laser wavelength depends on the injection current because it affects the diode temperature as well as the carrier density which in turn changes the index of refraction [73].

I constructed a temperature controller to stabilise the operating temperature and change it accordingly. Figure 4.6 shows how we decided the necessary stability required for the temperature controller. With the constructed temperature controller we can stabilise the temperature to better than 5 mK over periods of 3 hours; i.e. on average the drift of frequency of the laser from the atomic transition is about 3 MHz/min

compared to theoretical design of 1 MHz per min. That means we have about 3 minutes (compared to the theoretical value of 10 min) for the collection of data at each value of the magnetic field. However, I believe the discrepancy between the actual results and theory can be narrowed by covering the diode laser assembly from the air currents and reducing the optical feedback from the lens system. The temperature stability of the diode laser was checked by monitoring the output of the instrumentation amplifier and the temperature indicator. In the experiment, one should scan the magnetic field around the required values and integrate the repetitive Hanle signals.

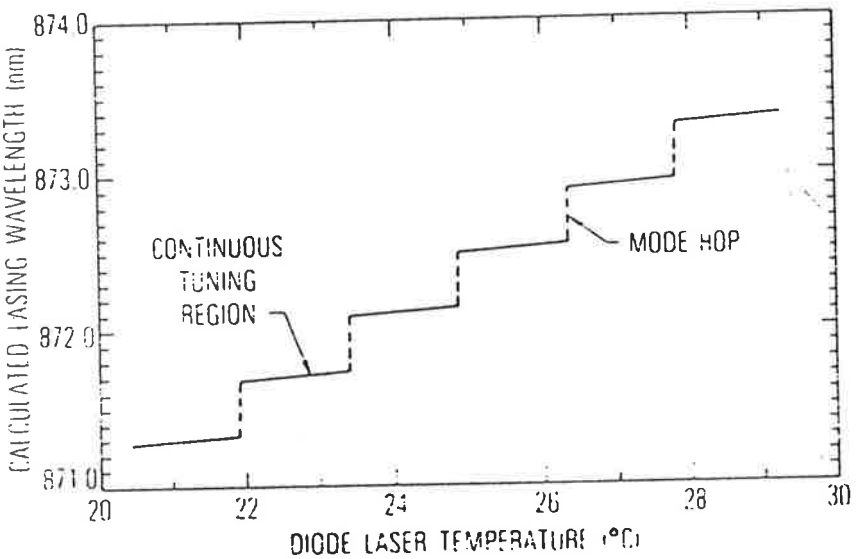

Figure 4.5: A typical tuning curve of the diode laser which shows the mode hopping regions. Mode hopping is usually undesirable in atomic physics studies as it is harder to tune the laser in resonance with the transition due to jumps in the laser wavelength and the increase in intensity noise accompanies the gain peak shift [74].

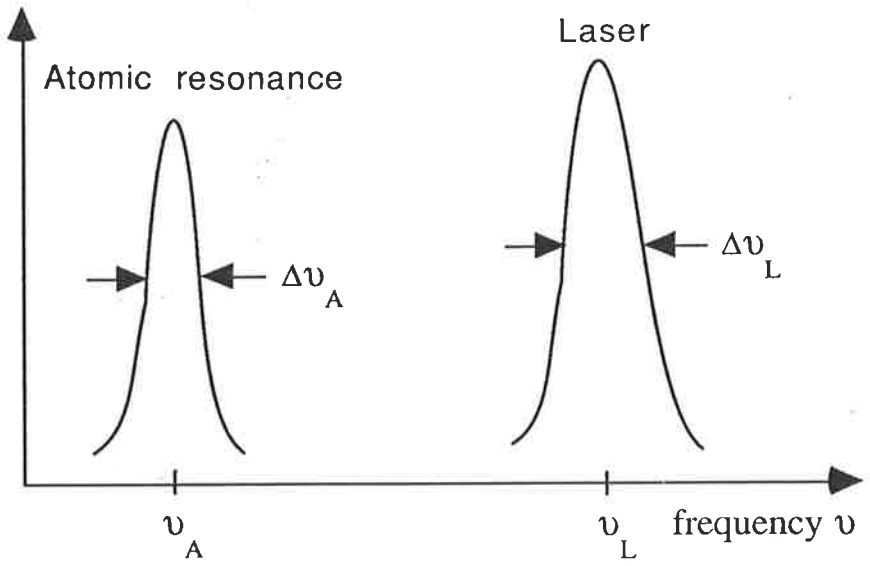

Figure 4.6: Laser must be tuned to resonance with the atom so that $|\upsilon_L - \upsilon_A| < \Delta\upsilon_L, \Delta\upsilon_A$. In the constructed geometry, the Doppler broadening is about 13 MHz (compared to natural width 0.14 MHz). Therefore the absorption width of the atomic transition is mainly determined by Doppler broadening (i.e. $\Delta\upsilon_A = \Delta\nu_D = 13$ MHz). The bandwidth of a typical free running diode laser is more than 30 MHz. Therefore we require $|\upsilon_L - \upsilon_A| \sim 9$ MHz. We decided the time taken for collection of data at each value of the magnetic field to be about 10 minutes. i.e. We design the temperature controller for a drift of about 1 MHz/min.

I started the technical design of the temperature controller by considering the problem of thermoelectric servomechanisms. The problem involves many details such as the mechanical stability of the mounting of the diode laser, the type of heatsink and heat pump and electronic configuration [75].

The mechanical design of the laser mount depends on several factors such as: dimension, mass, geometry and distance between temperature sensor, diode laser and heat sink. The time constant of the laser mount is also a important factor that should be taken into account. The time constant is defined as intrinsic time scale for which internal temperature differences decay away by heat conduction within the mount.

The construction of the laser mount was done in the mechanical workshop based on the design described by Mac Adam et al [76]. Figure 4.7 shows a schematic view of the laser mount together with its base plate in which the mount and the collimating lens is placed.

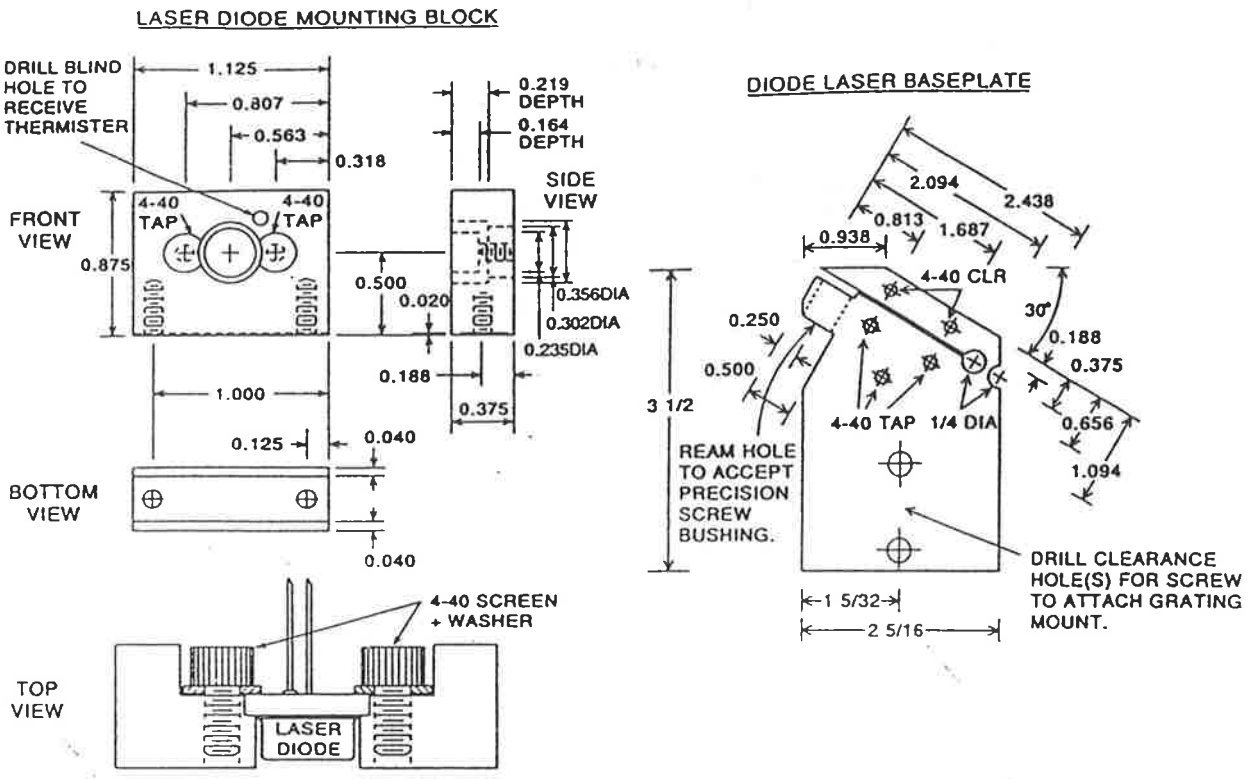

Fig 4.7: Schematic diagram of the laser mounting block and laser base plate (machine drawing) from reference [76].

The material used in the construction of the laser mount was aluminium as it is easy to machine, although from a consideration of the intrinsic time constant copper is preferred. The time constant of the aluminium mount is about 11 seconds while the time constant of a similar mount made with copper is 9.5 seconds.

In general the choice of the heat sink depends on the maximum temperature difference applicable in the experiment. The heat sink had a

surface area of 60 cm^2 and a thermal resistance 1.4 K/W. The heat sink performed well in the temperature range 10^o C to 55^o C. A Peltier thermoelectric heat pump Marlow model MI1064T was selected. The heat pump lies between the laser mount and the heat sink. It is important to make a very good thermal contact between the laser mount , the heat pump and the heat sink. We used a thermally conductive glue (with brand name Loctite) to make a good thermal contact. It is also important to isolate the diode laser and its mount from any electrical contact. I used nylon screws to connect the mount to the base plate. An insulator sheet also was placed between the mount and the base plate.

The electronic part of the servo system was constructed based on the design of C.C Bradley et al [77]. A fundamental part of the design is a thermistor sensing element (5K) as part of a Wheatstone bridge circuit. The position of the thermistor relative to the heat pump is an important factor in the response of the temperature controller, and its long term stability. The sensing thermistor was positioned in a small hole 2 mm from the heat pump in the diode laser mount. The block diagram of the temperature controller circuit which drives the heat pump is shown in figure 4.8. As we can see from the design, the circuit consists of a bridge, an instrumentation amplifier, a proportional stage, an integrator stage and the heat pump. A ten turn potentiometer selects the intended or desired " setpoint temperature". The voltage from the thermistor is compared with the setpoint voltage in a Wheatstone bridge which has a stable reference source LM299A (from National Semiconductor) as its supply (6.8V). The voltage difference which appears across the bridge is amplified 400 times by an Amp-01E instrumentation amplifier (manufactured by Precision Monolithics) with good common mode rejection of 130 dB. The output error signal is fed into a near unity gain proportional amplifier and a integrating amplifier which in combination control the current passing

through the heat pump. For an optimum performance of the temperature controller, I adjust the gains of the proportional and integrator stages. This damps out the feedback oscillations as quickly as possible. The ideal adjustment occurs when we achieve a critical damped situation. The detailed circuit diagram of the temperature controller is shown in appendix 4.

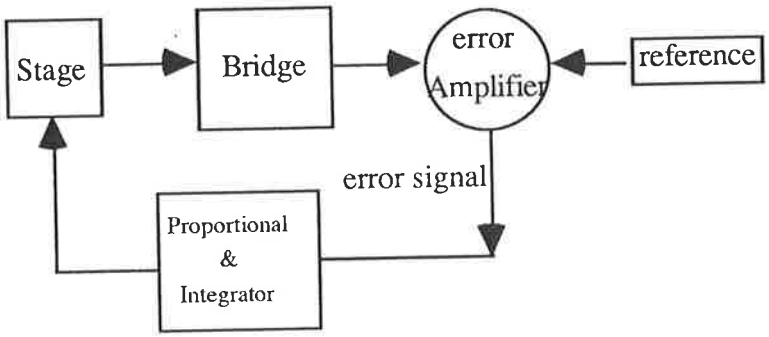

Fig 4.8: Block diagram of the temperature controller

The current driver was constructed in the electronic workshop based on the design by C.C Bradley et al [77]. The current driver delivers current up to 100 mA. Rechargeable lead acid batteries are used to supply power to the circuit in order to avoid mains line noise and transients.

4.3) Experimental set up and procedure

A commercial Sm-Ne hollow cathode discharge lamp from Photron was used for the calibration of the diode laser. A dc power supply Fluke model 412B was used to break down the neon gas in the discharge lamp. The applied voltage was of order 500 V. It includes the voltage drop across the ballast resistance and the discharge lamp. The pressure of the gas in the lamp was 1 Torr.

The OPG signals were measured via a change in the voltage across a variable ballast resistor (see fig 4.9 for the detection circuit). The transitions were monitored by an oscilloscope or a SR510 lock-in amplifier. A 0.1 μF capacitor protects the lock-in from the DC component of the discharge. A pair of diodes protects the input of the oscilloscope or lock-in amplifier from the AC voltage pulses. These pulses occur at the cathode when the discharge is started. The laser beam was modulated by a mechanical chopper. A signal from the chopper provides a reference frequency for the oscilloscope or the lock-in. All measurements reported here were taken at a chopping frequency of 385 Hz. The laser light is directed into the hollow cathode in most experiments. However sometimes the laser beam was directed perpendicular to the lamp axis between the anode and the cathode. In this case the signal amplitude sharply decreased.

A typical spectrum recorded by the OPG spectroscopy in the interval of 667.8nm up to 673.5nm is shown in figure 4.10. The spectrum was taken by scanning the diode laser temperature. The fine tuning of wavelength was done by tuning the current controller. After each scan, the unfocused diode laser was directed to a photodiode to check for any abnormal jumps in the laser beam. Such jumps for example can be attributed to the change in threshold level of the laser as the temperature changes .

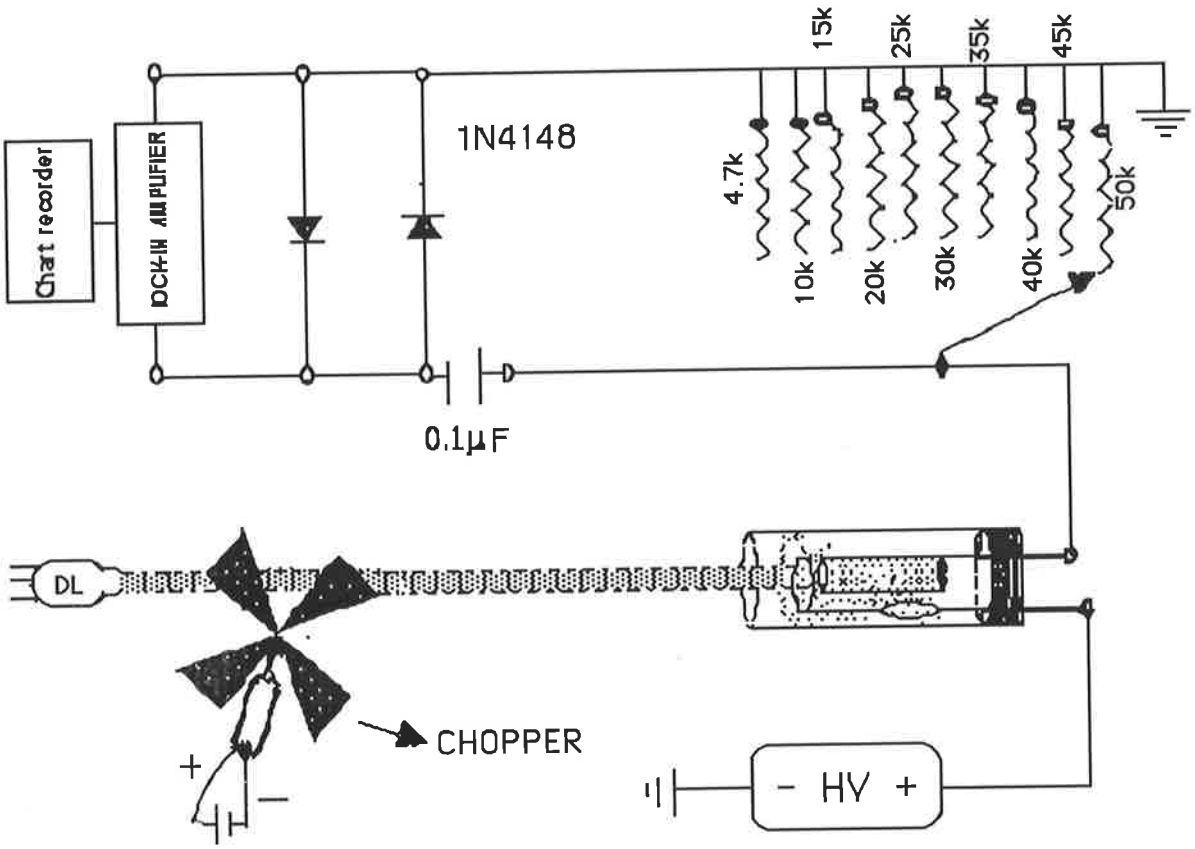

Figure 4.9: Block diagram of the optogalvanic detection system

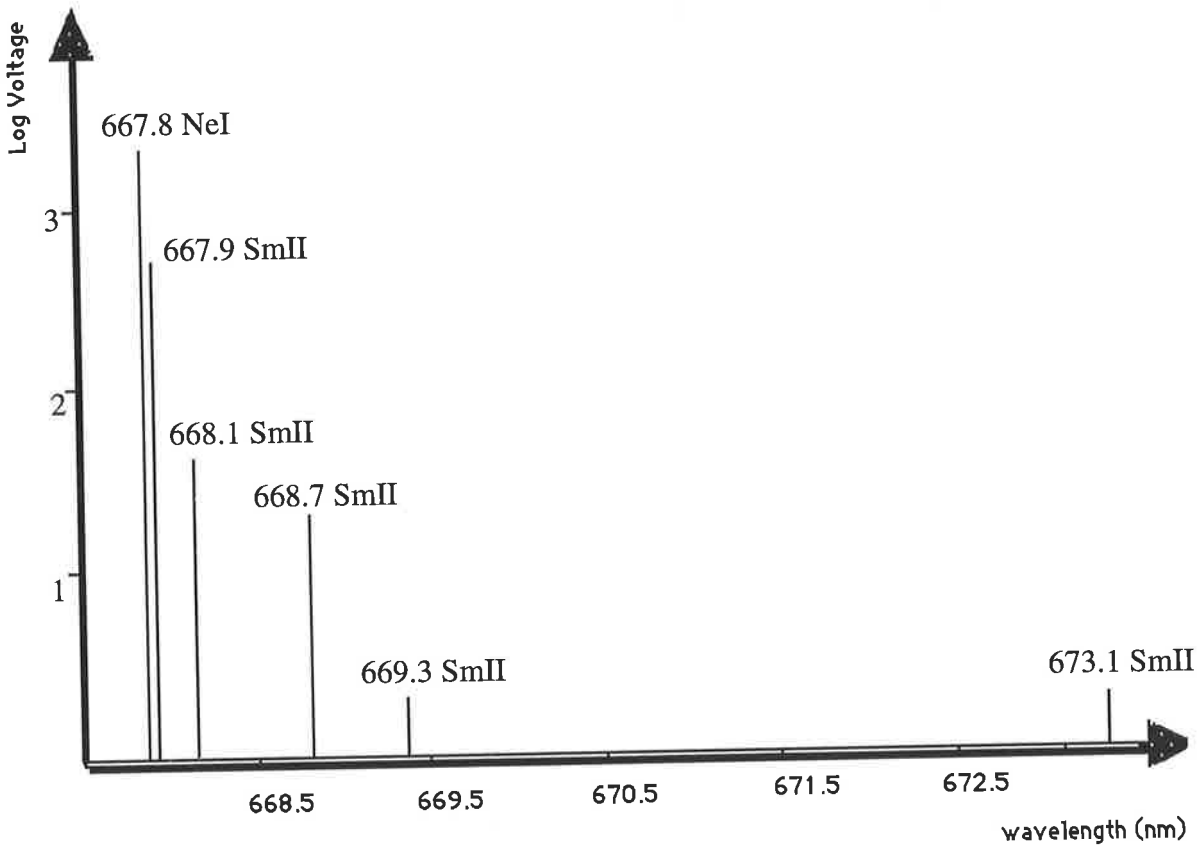

Figure 4.10: The wavelengths of the detected signal and their relative intensity by OPG spectroscopy.

From Ohms law one can deduce the minimum detection limits of the optogalvanic detection system of figure 4.9.

$$i = \frac{V_o}{R_B + R_D}$$

$$\because \Delta i = \frac{\Delta i^{R_D}}{\Delta R_D}\Delta R_D + \frac{\Delta i^{R_B}}{\Delta R_B}\Delta R_B$$

$$\therefore \Delta i = \frac{-V_o \Delta R_D}{(R_B + R_D)}$$

Here V_o is the constant voltage of the power supply, R_B is the ballast resistor, R_D is the resistor of the discharge, i is the current passing through the ballast resistor R_B, Δi is the change in the current of the circuit due to

the laser irradiation of the discharge, ΔR_D, ΔR_B are the corresponding changes in discharge resistor and ballast resistor respectively. Δi^{R_D} and ΔR^{RB} means differentiation with respect to RD and RB.

Inspection of the above equation shows that Δi and consequently ΔV depends on the value chosen for the ballast resistor and to the discharge resistor. Figure 4.11 shows the dependency of the ΔV on the ballast resistor. The discharge current was kept constant during the measurements by changing the voltage of the power supply.

It can be seen that for the 667.8 nm of Neon, the OPG effect increases with increasing ballast resistor and then drops to a minimum.
A further increase of ballast resistor values leads to a sharp increase in OPG Neon signal. The best signal can be obtained from the ballast resistor of 45 KΩ. The most probable explanation is that the electron production rate efficiency in the ballast resistor (corresponding to each photon absorbed in the discharge) depends on the value of the ballast resistor and to the voltage through the resistor.

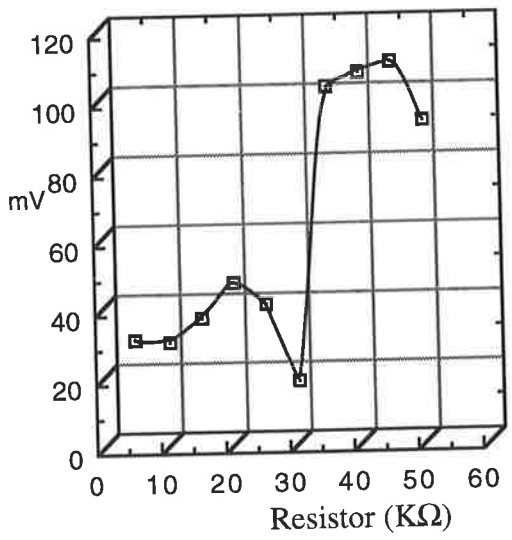

Figure 4.11: Dependency of the 667.8 nm Neon signal on ballast resistor. Discharge current was kept constant during the measurement.

The magnitude of the shot noise in the ballast resistor is the most important factor in the minimum detection limit. It can be evaluated by the expression [78]:

$$V_{sn} = 5.66 \times 10^{-10} R_B \sqrt{B_p i}$$

Where B_p is the bandpass frequency of the measuring apparatus.

For the bandpass of 20 kHz, at 10mA discharge current and 25 kΩ ballast resistor, the value for the shot noise is $V_{sn} = 1 \times 10^{-4}$ V (rms) .

Noise in OPG spectroscopy was measured by the method suggested by H.W Ott [79]. The method consists of using a variable bandpass filter and an oscilloscope to measure the noise across the ballast resistor as a function of frequency and bandpass. Then the peak to peak voltage measured on the oscilloscope is divided by eight to obtain the rms readings. The measured value for the shot noise is 0.2 mV comparable with the calculated value of 0.1 mV.

4.4) Data analysis

Table 4.1 lists all the transitions of Ne and Sm which lie in the accessible range of the diode laser. We detected 6 transitions from the list. The detection of other transitions would only be possible by using an external Fabry-Perot etalon as it allows us to select only a single mode output among many longitudinal modes of the diode laser.

wavelength nm	spectrum	Energy level cm^{-1}	transition
667.15	SmI	4017-19006	$^7F_6 \rightarrow {}^9F_7$
*667.80	NeI	13589-15086	$^1S_2 \rightarrow {}^2P_4$
* 667.92	SmII	8679-23647	$^8H_{9/2} \rightarrow {}^8F_{9/2}$
* 668.15	SmII	11359-26358	$^8G_{7/2} \rightarrow {}^8F_{5/2}$
* 668.77	SmII	13777-28725	$^6P_{7/2} \rightarrow {}^8H_{9/2}$
* 669.35	SmII	13604-28540	$? \rightarrow {}^8H_{11/2}$
669.46	SmII	11047-25980	$^6P_{3/2} \rightarrow {}^8F_{5/2}$
670.36	SmI	17655-32568	$^9D_6 \rightarrow {}^9F_7$
670.74	SmII	7525-22429	$^8H_{5/2} \rightarrow {}^8F_{5/2}$
671.26	SmII	12045-26938	$^8H_{7/2} \rightarrow {}^8G_{7/2}$
671.70	NeI	13589-15077	$^2S_2 \rightarrow {}^2P_5$
672.30 672.32	SmI	13050-27920	$^7H_2 \rightarrow {}^7D_2$
672.47	SmI	16859-31726	$^9D_5 \rightarrow {}^9F_6$
672.58	SmI	0-14864	$^7F_0 \rightarrow {}^9F_1$
* 673.18	SmII	9407-24257	$^8H_{11/2} \rightarrow {}^8F_{9/2}$
673.40	SmII	11094-25940	$^8H_{15/2} \rightarrow {}^8F_{13/2}$

Table 4.1: List of all transitions of Sm and Ne which lie in the accessible range of the diode laser. The marked transitions are the ones which we detected.

OPG spectroscopy was used to calibrate the laser wavelength with the temperature and the current of the diode laser. The resolution of OPG spectroscopy was 0.1 nm. Figure 4.12 shows the result of the wavelength calibration of the diode laser by OPG spectroscopy.

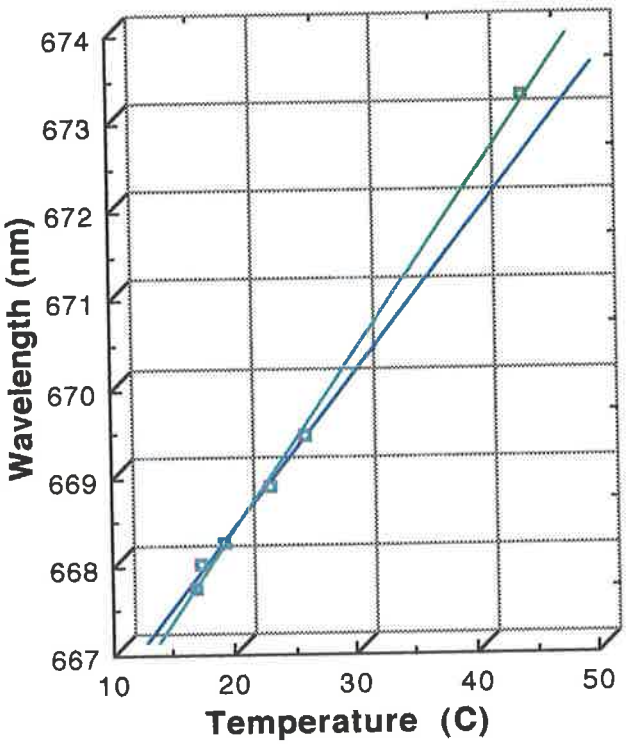

Fig 4.12: Calibration of the diode laser wavelength v.s temperature by OPG spectroscopy. Green curve shows the calibration when all the six point were present (5.0 deg per nm). Blue curve shows the calibration when we removed the 673.1 nm signal. In this case we calibrate the laser wavelength as 5.6 deg per nm. The size of the square denotes the error.

1) Detection of Neon lines

As one can see from the table 4.1 there are only 2 Neon lines in the wavelength range 667.5-673.5 nm. The OPG of the 667.8 nm always gives a negative signal of maximum amplitude 350 mV in the oscilloscope. Here, the situation corresponds to figure 3.6 a) in chapter 3. It is because the population of the excited level $2p_4$ which lies closer to the ionisation limit increases by laser excitation from $1s_2$ level and so the ionisation proceeds more rapidly from the higher state. This will result in

an increase in the conductance which corresponds to a negative voltage signal. Figure 4.13 shows a typical row data for 667.8 nm of Ne.

The transition 671.7 nm of Neon was not detected by optogalvanic spectroscopy. The reason might be that the tuning gaps in the tuning curve of the diode laser might occur exactly at the wavelength corresponding to 671.7 nm of Neon.

2) Detection of Sm lines

All the detected Samarium lines belong to the first ionisation state. A total of five Samarium lines were detected by the optogalvanic spectroscopy. There was no previous detection of these lines by optogalvanic spectroscopy. The 667.92 nm transition was strongest detected signal. The signal could be observed on the oscilloscope with an amplitude of about 50mV. The signal polarity was negative. (see fig 4.13).

The 668.15 nm signal was observed on the oscilloscope with a amplitude of about 4 mV. The signal from 668.77 nm line could also be observed on the oscilloscope. However the amplitude of the signal was only 2 mV. The signals 669.3 nm and 673.1 nm were detected by phase sensitive detection while we scanned the diode laser temperature around 18.3^{o}C and 45^{o}C, respectively. The signal to noise ratio for 673.1 nm line was two. The time constant of the lock in amplifier was set at 1s. The phase of the reference signal relative to the optogalvanic signal varied a few degrees due to the change in the chopping frequency. A typical raw data for the 673.1 nm transition is shown in figure 4.14. In figure 4.12 we also showed the calibration of the diode laser without 673.1 nm signal .

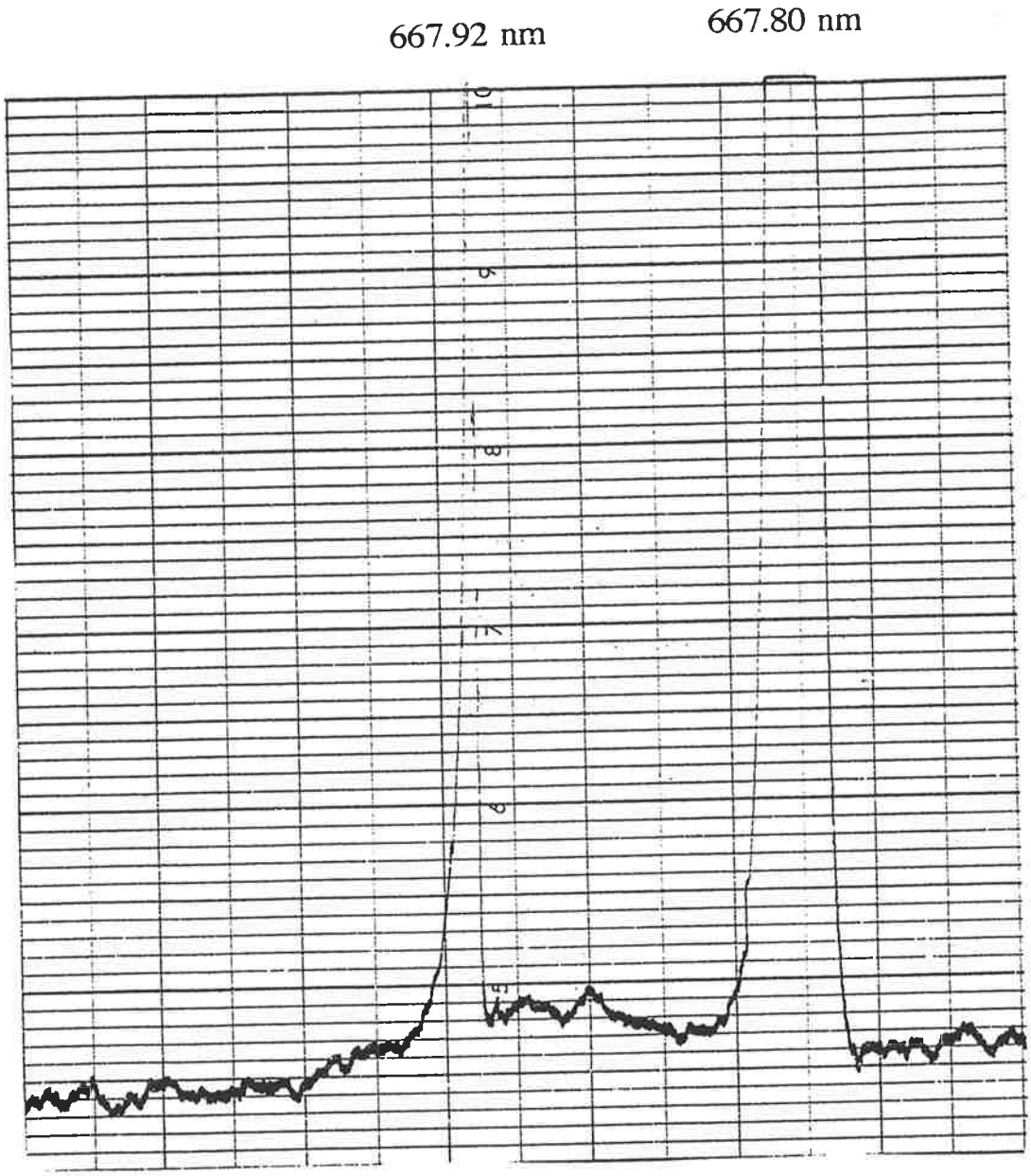

Figure 4.13: A Typical experimental run which shows 2 wavelengths: 667.80 nm of Neon and 667.92 nm of Sm. The data was taken under the following conditions: Diode laser current 40.3 mA , temperature 16.2 $^{\circ}C$, for Ne line and 16.7 $^{\circ}C$ for Sm line, Discharge current 10 mA and chopper frequency 385 Hz.

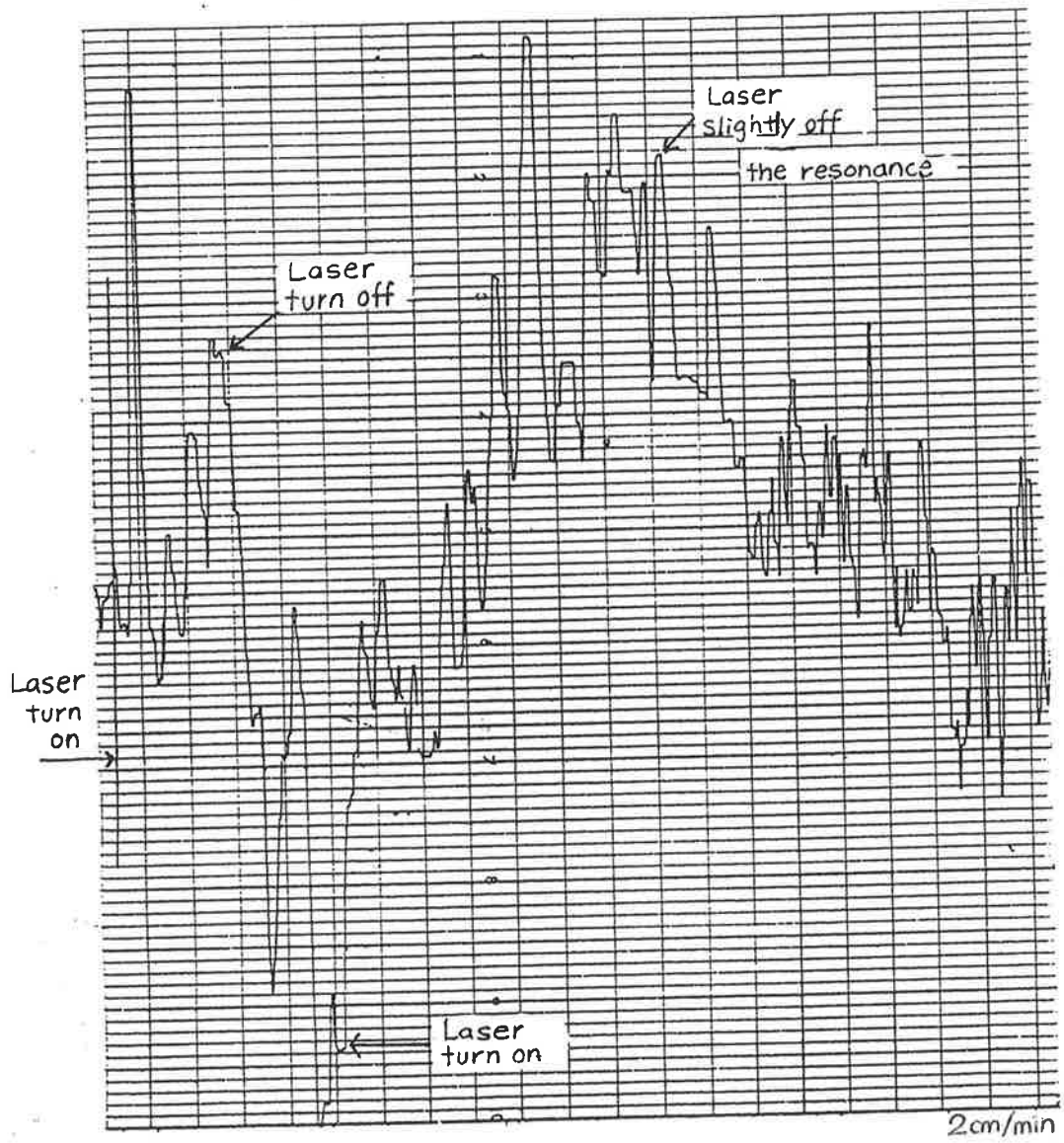

Figure 4.14: Typical raw data for the 673.1 nm transition which was the hardest signal to detect. The data was taken under the following conditions: Diode laser current 54.1 mA, Temperature 43.85 $^{\circ}C$, Discharge current 17.5 mA and chopper frequency 385 Hz.

4.5) Conclusion

We designed and constructed the apparatus for the measurement of the lifetime of the excited state of Samarium by the Hanle effect. All parameters which affect the shape of the Hanle signal were discussed. I also critically studied the collimation of the atomic beam and the possible sources of the transition line broadening. It was found the Doppler shift is the main source of the line broadening. In addition we suggest a new method for the detection of Sm atomic beam. The method was based on the reflection pulse technique of V. Dolocan as we describe in appendix 3. However, no attempt was made to test the method experimentally due to time constraint. Our constructed diode laser temperature controller fulfilled all the expectations. It will allow us to keep the laser in resonance with the transition over a periods of 3 minutes. That means, we have a time of about 3 minutes to collect data at each value of the magnetic field.

The OPG method was used to calibrate the diode laser wavelength. The wavelength resolution of the OPG spectroscopy was 0.1nm. The polarity of the experimental results were compared with the Samarium-Neon hollow cathode discharge modelling. From the model we correctly predicted the sign of the detected transitions. We also listed the conditions in which allow us to obtain line profiles which under certain conditions determine the laser bandwidth. The minimum detection limit of the optogalvanic technique was established from the shot noise in the ballast resistor. A noise level of 0.2 mV was measured in the ballast resistor. The first OPG of the Sm-Neon discharge in the region of 667.5 to 673.5 nm was recorded.

An important aspect of this experiment was the development of a experimental set up which allows simultaneous optogalvanic and fluorescence Hanle observations. As a result, the door was opened to future experiments involving CPT.

REFERENCES

[1] W. Hanle (1924) "Z Physics" Vol 30, P 93

[2] E. B. Alexandrove (1973) " Soviet physics Usp" Vol 15, No 4, P 436

[3] V. G. Pokozan'ev, G. V. Skrotskii (1973) "Soviet Physics Usp" Vol.15, No.4, P.452

[4] P. M. Pierre and M. Sargent (1991) "Elements of quantum optic" Springer-Verlagm Publisher

[5] E. B. Alexandrov, M. P. Chaika and G. I. Khvostenko "Interference of atomic States" Springer-Verlagm .

[6] M. W. Hamilton (1990) "Laser noise in non linear optical processes" Research proposal University of Adelaide

[7] G. Moruzzi and F. Strumia (1994) "Comments on atomic and Molecular Physics" Vol 29, No 6, P. 347

[8] R. J. McLean, R. J. Ballagh and D. M. Warrington (1985) " Journal of physics B: Atomic and molecular physics" Vol 18, P 2371

[9] M. B. Gornyi and B. G. Matisov (1989) "Opt. Spectrosc" Vol 66, No 5, P 567

[10] B. D. Agap'ev, M. B. Gornyi and B. G. Matisov (1993) "Reviews of Topical Problems Physics-Usp" Vol 36, No 9, P 763

[11] I. E. Mazets and B. G. Matisov (1992) "Soviet Physics JETP" Vol 74, No.1, P 13

[12] M. W. Hamilton and G. N. Sinclair (1994) " Review of scientific instruments" Vol 65, N0 6, P

[13] R. Mannella and P. V. E. McClintock (1990) " Contemporary Physics" Volume 31, No 3, P 179

[14] K. Ernst and M. Inguscio (1986) " Unconventional Techniques in Laser Spectroscopy" Vol 11, No 2

[15] A. Corney (1977) "Atomic & Laser Spectroscopy" Oxford

[16] G. Moruzzi and F. Strumia (1991) "The Hanle Effect and Level-Crossing Spectroscopy" Plenum press, New York

[17] P. W. Milonni and J. H Eberly (1988) "Lasers" John Wiley and sons

[18] B. W. Shore (1990) " The theory of coherent atomic excitation" Vol 1, John Wiley and sons

[18A] W. Demtroder (1981) " Laser spectroscopy" Springer- Verlag Berlin

[19] S. Svanberg (1991) " Atomic and Molecular Spectroscopy: Springer-Verlag Berlin

[20] U. Fano (1957) "Reviews of Modern Physics" Vol 29, No 1, P 74

[21] K. Blum (1981) " Density matrix theory and applications" Plenum press, New York

[22] M. G. Boshier, D. Berkeland, E. A. Hinds and V. Sandoghdar " physics department" Yale university , New york

[23] L. Allen and J. H. Eberly (1975) " Optical resonance and two level atoms" Vol XXVII, John Wiley and sons

[24] K. Arnett, S. J. Smith, R. E. Ryan, T. Bergeman, H. Metcalf, M. W. Hamilton and J. R. Brandenberger (1990) "Physical Review A" Vol 41, No 5, P 2580

[25] P. Avan and C. Cohen-Tannoudji (1975) "Le Journal De Physique" Vol 36, P L-85

[26] R. E. Ryan, T. H. Bergeman (1990) "Physical Review A" Vol 43, No 11, P 6142

[27] R. J. McLean (1982) " A study of laser induced Zeeman coherence in neon" PhD thesis, University of Otago, New Zealand

[28] W. Rasmussen, R. Schieder and H. Walther (1974) "Optics communications" Vol 12, No 3, P 315

[29] G. Orriols (1979) " Il Nuovo cimento" Vol 53B, No 1, P 1.

[30] M. W. Hamilton in reference [6] referred to McLean et al (1985)

[31] L. Marek (1978) " Astronomy and Astrophysics" Vol 62, P 245

[31a] Examiner suggestions

[32] M. R. Law (1994) " Electron Scattering from calcium" PhD thesis Flinders university.

[33] G. Scoles (1992) " Atomic and Molecular beam methods" Vol 2, Oxford University Press, See chapter 7 page 218 .

[34] Private conversation With D. G. McCoy (1995) University of Adelaide

[35] A. E. Ruark and M.F. Peters (1926) " Journal of the optical society of America and Review of scientific Instruments" Vol 13, P 205

[36] R. K. Cacak and J. R. Craig (1969) " Review of scientific instruments" Vol 40, No 11, P 1468

[37] A. Aspect, E. Arimondo, R. Kaiser, N. Vansteenkiste and C. Cohen- Tannoudji (1988) " Physical Review Letters" Vol 61, P 826

[38] I. E. Mazets and B.G Matisov (1994) " JETP letters" Vol 60, No 10 P 703

[39] F. M. Penning (1928) "Physica" Vol 8 , P 137

[40] E. M. Van Veldhuizen, F.J. de Hoog, and D.C Schram (1984) " Journal of Applied physics" Vol 56, No 7, P 2047

[41] J. E. M. GoldSmith and J. E. Lawler (1981) " Contemp. Phys" Vol 22, No 2, P 235

[42] R. A. Keller, B. E. Warner, E. F. Zalewski, P. Dyer, R. Englemann and B. A Palmer (1983) " Journal de Physique" Colloque c7, P 23

[43] A. J. Stirling (1969) " spectroscopic studies in shock tubes and sputtering discharges" Phd thesis, flinders university

[44] J. R. Nestor (1982) " Applied Optics" Vol 21, No 22, P 4154

[45] P. Hannaford and G. W. Series (1981) "J. Phys B" Vol 14, P L661

[46] S. Yamaguchi and M. Suzuki (1982) "Applied Physics Letters" Vol 41, No 7, P 597

[47] G. C Turk, J. C. Travis and J. R. Devoe (1983) " Journal de Physique" Colloque C7, P 301

[48] I. Popescu and N. Geuusescu (1983) " Journal de physique" Colloque C7, P 3

[49] D. A. Swift (1981) " Contemporary physics" Vol 22, No 1, P 37

[50] R. Mavrodineau (1984) "Journal of research of the national Bureau of Standards" Vol 89, No 2, P 143

[51] B. Barbieri and N. Beverini (1990) "Reviews of Modern Physics" Vol 62, No 3, P 603

[52] N. S. Kopeika, J. Rosenbaum and R. Kastuer (1976) " Applied Optics" Vol 15, No 6, P 1976

[53] Y. P. Raizer (1991) " Gas Discharge Physics" Springer-Verlag Pub

[54] J. T. Verdeyen (1989) "Laser electronics" Englewood Cliffs Publication

[55] B. Visentin, F.Harrault, R. Gobin, and P.A. Leroy (1994) " Review of Scientific Instruments" Vol 65, No 4, P 1129

[56] M. E. Pillow (1981) "Spectro Chimica Acta" Vol 36B, No 8, P 821, See page 823, 837

[57] B. J. Russell and A. Walsh (1959) " Spectro Chimica Acta" Vol 10, P883

[58] C. PopoVici and M. Somesan (1965) " Electronic letters' Vol 1-2, P 31

[59] V. N. Ochkin, N. G. Preobrazhenskii, N. N Sobolev and N. Ya. Shparev (1986) "Soviet Physics Usp" Vol 29, No 3, P 260. Reference to E. M. Veldhuism

[60] K. Arnett, R. Anderson and R. Alexander (1981) " American journal of physics" Vol 49, No 8, P 767

[61] W. C. Martin, R. Zalubas and L. Hagan (1976) "Atomic Energy Levels-The Rare-Earth Elements" National Bureau of Standard USA

[62] W. F. Meggers, C. H. Corliss and B. F. Scribner (1975) "Tables of Spectral lines- Arranged by elements" NBS monograph 145 part 1, US Government printing office

[63] I. Estermann (1946) "Reviews of modern Physics" Vol 18, No 3, P 300

[64] A. H. Firester (1966) " Review of Scientific Instruments" Vol 37, P 1264

[65] R. M. Park and H. M. Hoersch(1993) " Manual on the use of thermocouples in temperature measurement" fourth edition, ASTM committee E20 on temperature measurement" American Society for testing and materials

[66] N. F. Ramsey (1956) " Molecular beams" Clarendon press, oxford

[67] W. Hanle and H. Kleinpoppen (1979) " Progress in atomic spectroscopy" Part B, Plenum press, New york

[68] P. Hannaford, P. L. Larkins and R. M. Lowe (1981) " Journal of physics B: Atomic and molecular physics" Vol 14, P 2321

[69] V. A. Komarovskii, N. P. Penkin and G. P. Nikiforova (1970) " Optics spektrosk" Vol 29, P220

[70] K. B. Blagoev, V. A. Komarovskii, and N. P. Penkin (1977) "Opt. Spectrosc" Vol 42, No 3, P 238

[71] P. Hannaford and R. M. Lowe (1985) " J. Phys. B: Atomic and Molecular Physics" Vol 18, P 2365

[72] J. C. Comparo (1985) " Contemp Phys" Vol 26, No 5, P 443

[73] C. E. Wieman and L. Hollberg (1991) " Review of Scientific Instruments" Vol 62, No 1, P 1

[74] D. J. Hodgson (1994) " Laser focus World" P129

[75] D. A. Van Baak (1992) " American Journal of physics" Vol 60 No 9, P 803

[76] K. B. Mac Adam, A. Steinbach and C. Wieman (1992)" American Journal of physics" Vol 60, No 12, P 1098

[77] C. C. Bradley, J. Chen and R. G. Hulet (1990) "Review of Scientific instrument" Vol 61, No 8, P 2097

[78] R. A. Keller and E. F. Zalewski (1980) "Applied Optics" Vol 19, No 19, P 3301

[79] H. W. Ott (1976) "Noise reduction techniques in Electronic systems" John Wiley and Sons New York

Appendix 1) Derivation of the steady state solution of the density matrix for a (J=0 to J=1) V-system

The time evolution of the matrix elements of ρ can be written in the following form:

$$
\begin{aligned}
i\dot{\rho}_{++} &= w(e^{-i\omega t}+e^{i\omega t})\rho_{0+} - \rho_{+0}w(e^{i\omega t}+e^{-i\omega t}) + i\Gamma\rho_{++} \\
i\dot{\rho}_{--} &= w(e^{-i\omega t}+e^{i\omega t})\rho_{0-} - \rho_{-0}w(e^{i\omega t}+e^{-i\omega t}) + i\Gamma\rho_{--} \\
i\dot{\rho}_{+-} &= -2\omega_l\rho_{-+} + w(e^{-i\omega t}+e^{i\omega t})\rho_{0+} - \rho_{-0}w(e^{i\omega t}+e^{-i\omega t}) + i\Gamma\rho_{-+} \\
i\dot{\rho}_{00} &= w(e^{i\omega t}+e^{-i\omega t})\rho_{+0} - \rho_{0+}w(e^{-i\omega t}+e^{i\omega t}) + w(e^{i\omega t}+e^{-i\omega t})\rho_{-0} + i\Gamma(\rho_{++}+\rho_{--} \\
i\dot{\rho}_{0+} &= -\rho_{0+}(\omega_o+\omega_l) + w(e^{i\omega t}+e^{-i\omega t})(\rho_{++}-\rho_{oo}-\rho_{-+}) + i\frac{\Gamma}{2}\rho_{0+} \\
i\dot{\rho}_{0-} &= -\rho_{0-}(\omega_o-\omega_l) + w(e^{i\omega t}+e^{-i\omega t})(\rho_{--}-\rho_{00}-\rho_{+-}) + i\frac{\Gamma}{2}\rho_{0-}
\end{aligned}
$$

(A1.1)

We can adopt the following solutions

$$
\begin{aligned}
\rho_{0+} &= \sigma_{0+}e^{i\omega t} \\
\rho_{+0} &= \sigma_{+0}e^{-i\omega t} \\
\rho_{0-} &= \sigma_{0-}e^{i\omega t} \\
\rho_{-0} &= \sigma_{-0}e^{i\omega t} \\
\rho_{00} &= \sigma_{00} = 1-(\sigma_{++}+\sigma_{--}) \\
\rho_{++} &= \sigma_{++} \\
\rho_{--} &= \sigma_{--} \\
\rho_{+-} &= \sigma_{+-}
\end{aligned}
\qquad \text{(A1.2)}
$$

to transform the above differential equations to a set of time independent differential equations. We also use rotating wave approximation: i.e. we can ignore the $e^{+2i\omega t}$ and $e^{-2i\omega t}$ terms from the time evolution equations as these terms oscillate much faster compare to the optical frequency ω and ω_l. Finally we will get:

$$\dot{\sigma}_{++} = -iw(\sigma_{0+} - \sigma_{+0}) - \Gamma\sigma_{++}$$
$$\dot{\sigma}_{--} = -iw(\sigma_{0-} - \sigma_{-0}) - \Gamma\sigma_{--}$$
$$\dot{\sigma}_{00} = iw(\sigma_{+0} - \sigma_{0+} + \sigma_{-0} - \sigma_{0-}) + \Gamma(\sigma_{++} + \sigma_{--})$$
$$\dot{\sigma}_{-+} = -2i\omega_l\sigma_{-+} + iw(\sigma_{0+} - \sigma_{-0}) - \Gamma\sigma_{-+}$$
$$i\omega\sigma_{0+} + \dot{\sigma}_{0+} = -i(\omega_o + \omega_l)\sigma_{0+} + iw(\sigma_{++} - \sigma_{00} - \sigma_{-+}) - \frac{1}{2}\Gamma\sigma_{0+}$$
$$i\omega\sigma_{0-} + \dot{\sigma}_{0-} = -i(\omega_o - \omega_l)\sigma_{0-} + w(\sigma_{--} - \sigma_{00} - \sigma_{+-}) - \frac{1}{2}\Gamma\sigma_{0-}$$

(A1.3)

For a steady state solution we set time derivatives to zero and look for the solutions when $\omega = \omega_o$:

$$\sigma_{++} = \frac{-iw(\sigma_{0+} - \sigma_{+0})}{\Gamma}$$
$$\sigma_{--} = \frac{-iw(\sigma_{0-} - \sigma_{-0})}{\Gamma}$$
$$\sigma_{-+} = \frac{-iw(\sigma_{0+} - \sigma_{-0})}{(\Gamma - 2i\omega_l)}$$
$$\sigma_{0+} = \frac{iw(2\sigma_{++} - 1 - \sigma_{--} - \sigma_{-+})}{(\frac{\Gamma}{2} + \omega_l)} \qquad \text{(A1.4)}$$
$$\sigma_{0-} = \frac{iw(1 - 2\sigma_{--} - \sigma_{++} - \sigma_{+-})}{(\frac{\Gamma}{2} + \omega_l)}$$

P Avan and C Cohen-Tannoudji [22] found the fluorescence signal $L_f(e_y)$ along the x-direction as:

$$L_f(e_y) \propto \sigma_{++} + \sigma_{--} + 2Re\sigma_{+-} \qquad \text{(A1.5)}$$

$$\sigma_{++} = \frac{w^2(\sigma_{+-} - \sigma_{-+})}{(\frac{\Gamma^2}{2} + \Gamma\omega_l)}$$

$$\sigma_{--} = \frac{w^2(\sigma_{-+} - \sigma_{+-})}{(\frac{\Gamma^2}{2} + \Gamma\omega_l)}$$

Reinserting the steady state values of $\sigma_{++}, \sigma_{--}, \sigma_{+-}$ into the equation (A1.5) and after a tedious but straightforward algebraic manipulation, one can finally get the following theoretical expression for the fluorescence signal $L_f(e_y)$ for the case of zero detuning:

$$L_f(e_y) = \frac{4\alpha\omega_l^2 w^2 F^2}{4w^2\omega_l^2(\alpha F + w^2 + 3\alpha^2) + \Gamma^2 F(Fw^2 + \alpha(4F + \alpha\omega_l^2 + w^2 + 4\alpha) + 4\alpha^3\omega_l^2}$$

where $\alpha = (\frac{\Gamma}{2})^2 + \omega_l^2$ and $F = \alpha + w^2$

Appendix 2)

For the geometry described in the main text, the Rabi frequency is given by [24].

$$w = \frac{deE_o}{\hbar\sqrt{2}}$$

where $$E_o^2 = \frac{2I}{c\varepsilon}$$

and $$d^2 = \frac{3\pi\varepsilon c^3\hbar}{e^2\tau\omega_o^3}$$

$$\omega_o = \frac{2\pi c}{\lambda}$$

then

$$w^2 = \frac{6\lambda^3 I}{16\pi^2 \hbar c \tau}$$

Unit Saturation happens when $1 = 2w^2\tau^2$, one will get

$$I_s = \frac{\pi hc}{3\lambda^3 \tau}$$

since $$\hbar = \frac{h}{2\pi}$$

Appendix 3)

Detection of Sm beam by Reflection pulse technique

Introduction

In transmission line theory it is an established fact that when an ideal transmission line (i.e. a uniform, lossless, dispersionless line) is terminated with an impedance equal to its characteristic impedance Z_o, (the ratio of the voltage to the current at every point of the line) there are no reflected waves on the line and the impedance at any point of the line is also equal to the line characteristic impedance.

However, when the ideal transmission line is not terminated with its characteristic impedance, but is terminated with some arbitrary impedance there are always reflected waves on the line, and the impedance at every point of the line differs from the characteristic impedance Z_o.

Here, we suppose the generator is matched to the line and only consider the reflection from the load end which is not terminated properly. In this case the relation of the reflected wave to the incident wave at every point of the line is determined by the nature of the load. The ratio of the voltage of the reflected wave (V_{ref})to the voltage of the incident wave (V_{in}) is called the reflection coefficient [1,2,3,4].

$$\rho_r = \frac{V_{ref}}{Vin} = \frac{Z_{ref} - Z_o}{Z_{ref} + Z_o}$$

where Z_{ref} is the load impedance which determines the shape of the reflective wave. We now look to some special cases of load termination. The mathematical derivation has appeared in many text on transmission lines and we only note the results.

Case 1)

The transmission line C_1 is terminated in an infinite load resistance and driven by a generator modelled as a voltage source in series with a resistance R_g equal to the characteristic impedance Z_o. The driving voltage consists of rectangular pulses of amplitude V_p and duration T_p. The same generator output is connected by second transmission line C_2 to a oscilloscope. The ends of the transmission line C_2 are matched to the pulse generator and the oscilloscope.

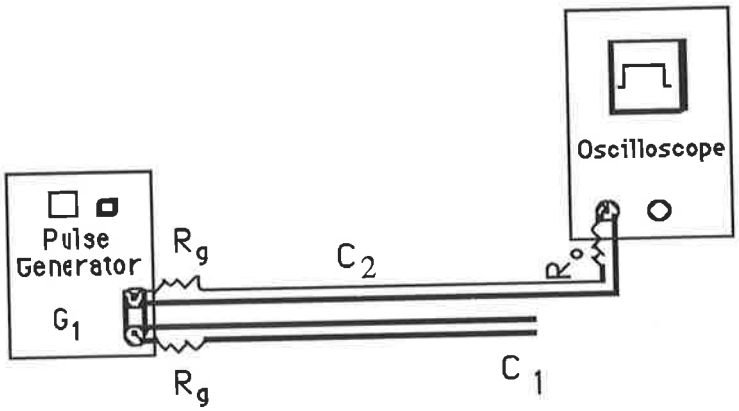

Fig 1: Termination at open circuit

Since for the open circuit of figure 1, $Z_{ref} = \infty$ therefore

$$\rho_r = \frac{Z_{ref} - Z_o}{Z_{ref} + Z_o} = +1$$

i.e. The reflected Voltage is equal to the incident voltage with the same sign. (see table 1a)

Case 2) Short circuit

We assume the same conditions as in case 1 with the difference that the end of cable C_1 is short circuited (See figure 2). In this case the reflected voltage is equal to the incident voltage but of opposite sign (see table 1b). The reflection coefficient r is equal to -1.

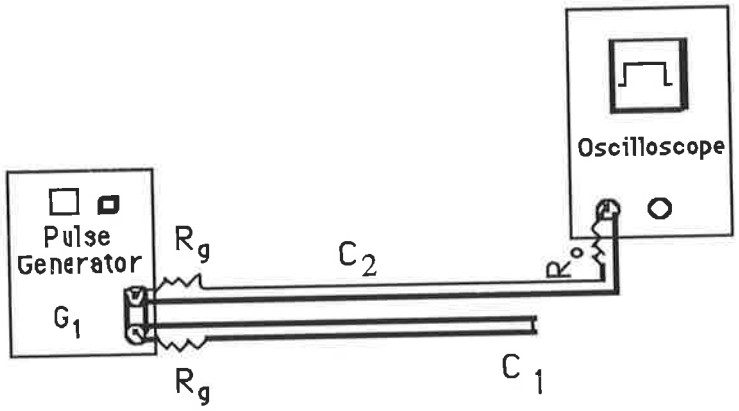

Fig 2: Short circuit termination

case 3) Line with reactive load

If the load is purely reactive, either inductive or capacitive, it will not consume any energy. As a result the amplitude of the reflected wave is the same as direct wave. (we assume Z_o is real). The reactive load, however, is able to store energy for a certain time and then return to the line as a reflected wave that is not in phase with the direct wave.

case 4) general case

The terminating load can be any combination of resistor and reactive components. In general case, the load impedance is a complex quantity. A discussion about the shape of reflected wave for all the different load

combinations is beyond the scope of this work. Table 1 only shows the typical shape of the reflected wave for different load termination related to this work.

Reflection pulse technique

Since the reflected signal (voltage) depends on the impedance characteristics of the terminating end of the transmission line, a change in the load impedance would effect the shape of the reflected wave.
Dolocan used the above fact to develop the reflection pulse technique. The method is very straight forward. A sample of a certain magnetic material is placed in the core of an inductive coil in series with a resistor. As the temperature of the sample is changed, the permeability of the magnetic material and also the inductance of the coil changes. The change in the inductance of the coil results in a change of the shape (width) of the reflected beam and this can be measured using a sampling oscilloscope [5,6,7].

We used the Dolocan pulse technique to detect the Sm while deposited in the core of an inductive coil. The detection circuit is shown in figure 3. The only difference between the Dolocan method of measuring permeability of the magnetic materials and our method of detection of Sm atomic beam is that Dolocan tried to measure the change in the inductance as the permeability of the sample changed while we tried to measure the change in the inductance as the number of particles changed. In appendix 1, we prove that the inductance of a coil is proportional to the amount of magnetic material deposited in the core.
A typical Sm atom has a permanent magnetic moment with a magnitude of m=1.6 μ_B where μ_B is the Bohr magneton .

The inductance of a coil, which has its core filled with material of uniform permeability μ, is given by

$$L_f = \frac{\mu N^2 s}{l}$$

where N is the number of turns of the coil, l is the length of the coil, S is the cross section area of the coil.

The inductance of an empty coil is given by:

$$L_e = \frac{\mu_o N^2 s}{l} \text{ where } \mu_o = 4\pi \times 10^{-7} \text{ Hm}^{-1}.$$

If the material doesn't fill all the coil core, then the inductance is given by

$$L = \frac{\mu N^2 s}{l} F + \frac{\mu_o N^2 s}{l}(1 - F) \qquad (1)$$

where F is the ratio of the volume of the core filled by the Sm to the whole of the core.

The inductance can be found from the reflection pulse technique. The rectangular generator is used to input voltage to coaxial cable c1 which is terminated by a coil of inductance L in series with a resistor R_T . The same generator output is connected to a sampling oscilloscope through a second cable C2. The generator output is matched to both the lines C1 and C2. The Sampling oscilloscope is also matched to the cable by a resistor R_S equal to the characteristic impedance of the line.

The reflected pulse of such system is shown in table 1.

The amplitude of the reflected pulse can be found from the expression

$$U = \{(\rho_r + (1 - \rho_r))e^{-(t-2T)/\tau}\}\{(U_o\Theta(t-2T) - e^{t_o/\tau}U_o\Theta(t - t_o - 2T)\}$$

$$\rho_r = \frac{R_T - Z}{R_T + Z}$$

$$\tau = \frac{L}{R_T + Z}$$

$$\Theta(t - x) = \{^{0, t<x}_{1, t>x}$$

Where t_O is the pulse width, 2T is the time delay of the reflected pulse against the direct pulse, Z is the impedance of the coaxial cable and U_O is the pulse amplitude at t-2T=0 defined in fig 4.2.2 (c). If $R_T << Z$ and t-2T=to (the pulse width), then we can measure U_1 and U_0 and determine t:

$$\tau = \frac{t - 2T}{\ln\{2/[(U_1/U_o)+1]\}} \tag{2}$$

and therefore

$$L = \tau Z \tag{3}$$

furthermore, if U1=0 Then

$$\tau = \frac{t_o}{\ln 2} \tag{4}$$

The minimum detection limit of the technique is determined by the time base of the laboratory oscilloscope. The sensitivity of the time base of the laboratory oscilloscope is 10 ns/cm; i.e. we can measure a change in the reflected pulse width t_0 of about 1 ns (corresponding to 1mm oscilloscope scale). The impedance of the coaxial cable is 50 Ω . The coaxial has a resistance R_T=0.1Ω in series with it. Since the condition $R_T << Z$ is fulfilled, then one can measure a variation in the inductance of about 0.1 mH. I have used equations 3 and 4.

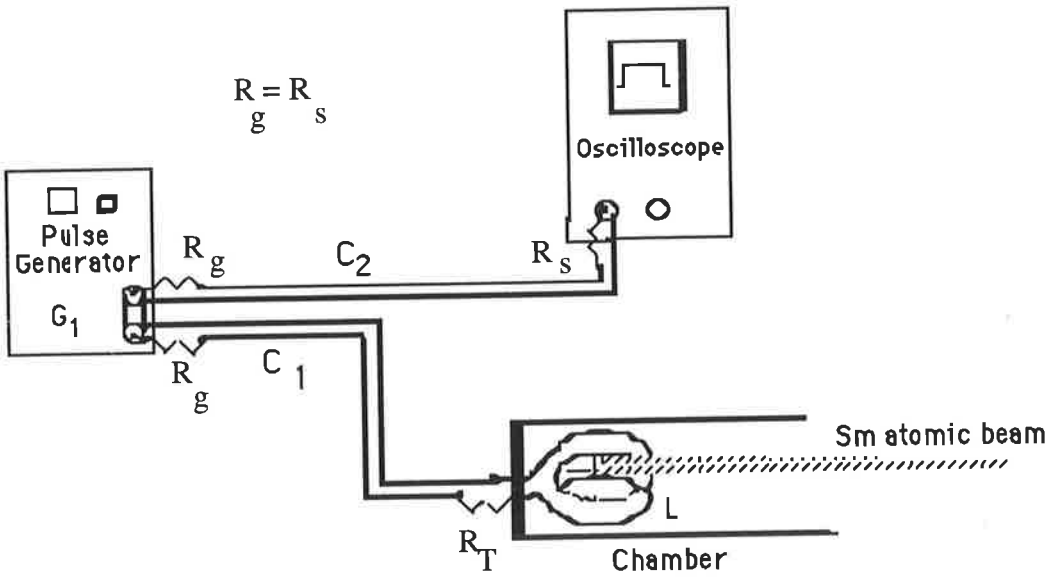

Fig 3: Detection of the Sm by the reflection pulse technique. Sm should be deposited along the axis of the coil. In actual experiments the coil illustrated above should be rotated.

The minimum detection thickness of Sm can be found from equation 1. Approximately, one can measure a minimum thickness of 5000 atoms (i.e. a thickness of 1.4 μm) for the following coil dimensions: N= 9 turns, l = 2 cm, S= πr^2 where r=2.5mm is the radius of the core. Samarium is deposited into a circular plate made of insulating materials. The radius of the plate is the same as the coil radius. We choose a relative permeability $\mu_r = \frac{\mu}{\mu_o} = \frac{L_f}{L_e} = 11$. Since Sm is a paramagnetic material at room temperature, it is necessary to find the temperature range in which μ_r>10. From equation 1 it is also evident that, the lower the permeability of the material, the more accurate the dimension of the coil should be chosen. I choose the dimensions of the coil such that it produces a uniform field in its centre and is also easy to build.

Dolocan measured a relative permeability of as low as 0.8 for a sample of 30 mm thickness by the reflection pulse technique.

Errors

In the detection of Sm by the reflection pulse technique, we measure the change in the inductance of a coil which contains the deposited Sm on its core. The reflected beam which contains the information about these changes travels along the coaxial cable. It is possible the shape of the reflected pulse changes along the coaxial cable due to attenuation and dispersion. It is therefore important to know the dielectric properties of the coaxial cable well in advance.

The other source of the error is actual size of the coil. In the construction of the coil, one should take great care in measuring the coil dimensions.

Suggested steps for the possible experiment

1) Select the Sampling oscilloscope and note its frequency and time response.

2) choose the pulse generator and the type of coaxial cable.

3) Design the dimensions of the coil for the minimum detection.

4) Build the coil carefully as designed.

5) Place the insulator inside the coil and put the assembly in the chamber. Choose the series resistor and place it outside the chamber. If necessary construct a cooling system inside the chamber to cool down the atomic beam.

6) set up the system.

7) Send nanosecond pulses into the coaxial cable. Choose carefully the repetition frequency of the pulses.

8) Determine the inductance of the empty coil in the chamber from the reflected width of the signal. If the reflected pulse length is smaller than the direct pulse length , then the case is related to table 1(d); i.e. $u_1=0$ and so we can use equation 4. Otherwise use equation 2 to determine t.

9) If you do not have the data related to permeability of the sample for different temperatures, then produce the data using the reflection pulse technique described by Dolocan.

9) Skip the step 8 if you aren't worried about the amount of deposition and the skin depth is larger than the sample thickness. The method works for all materials in which their permeability $\mu_s > \mu_o (\mu_r > 1)$.

10) Repeat the procedure 7 for different temperatures. With changing temperature, the rate of deposition will change and hence the width of the reflected wave will also be changed. From the graph of the reflected width versus oven temperature one can deduce the information regarding the intensity of the beam.

Conclusion

Reflection pulse technique is a method developed by Dolocan to measure the temperature dependency of the permeability of the magnetic material. We extend the application of the method to detect the atomic beam of Paramagnetic materials. For Sm, we are able to show that we can detect 5000 atoms thick for an assumed relative permeability of 10. However a setback for the method is that we should first determine the temperature range over which the permeability of samarium is bigger than 10.

In conclusion, I would like to suggest that the experts look for possible applications of the reflection pulse technique for the detection of the atomic beams of materials (which have a relative permeability higher than 1 at room temperature).

References

[1] R.E. Matick (1969) "Transmission lines for digital and communication networks" Mc Graw Hill Inc New York

[2] I.A.D Lewis and F.H. Wells (1954) " Millimicrosecond pulse technique Pergamon press Ltd London

[3] F.E Terman (1951) " Electric transmission lines" Mc Graw Hill Inc New york

[4] H. A. Hauss and J.R. Melchess (1989) " Electromagnetic fields and energy" Prentice Hall International

[5] V. Dolocan (1992) " measurement science and technology" no 3, P 366

[6] V. Dolocan (1994) " Review of scientific instrument" Vol 65, no 11, P 3505

[7] V. Dolocan and E Dolocan (1994) " Journal de physique III" Vol 4, No 10, P 1901

Case	Description	Direct pulse	Reflected pulse
a	Open circuit $z=\infty$		
b	Short circuit $z=0$		
c	Series resistance and inductance $\tau < t_o$		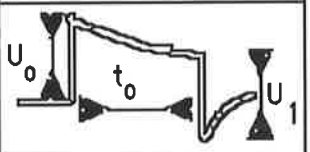
d	Series resistance and inductance $\tau > t_o$		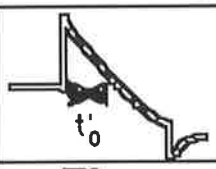
e	Parallel resistance and inductance		

Table 1) The shape of the reflected pulse for different terminations.

Appendix 1)

To prove the inductance of a magnetic coil depends on the amount of magnetic material which is deposited in its core, we use the definition of the inductance [4]:

$$L = \frac{\int_s \mu H . da}{i}$$

where

i is the current in the coil,

H is the magnetic field intensity inside the coil,

μ is the permeability of the materials of the core,

da is the surface area element of surface s.

For a linear magnetic material

$$H = \frac{M}{\chi_m}$$

where χ_m is the magnetic susceptibility and M is the magnetisation and is equal to

$$M = \frac{\Sigma m_i}{\Delta V}$$

where Σm_i is the vector sum of the magnetic moments over the atoms or molecules in the volume element ΔV of the materials.

For Sm, all the atoms in the beam have the same magnetic dipole moment m, therefor $\Sigma m_i = nm$

where n is the number of atoms deposited in the core.

Therefore L can be written as:

$$L = \int_s \frac{\mu}{\chi_m} \frac{nm}{\Delta V}$$

i.e. L is proportional to n

Appendix 4)

Schematic of the temperature controller which can stablise temperature to better than 5 mK